Human effector CD8$^+$ T cells with an exhausted-like phenotype control tumor growth *in vivo* in a humanized tumor model

Juliane Mietz[1], Meike Kaulfuss[1], Lukas Egli[1], Lennart Opitz[2],Christian Münz[3], Obinna Chijioke[1,4]

[1]Cellular Immunotherapy, Institute of Experimental Immunology, University of Zürich, Zürich, Switzerland
[2]Functional Genomics Center Zürich, University of Zürich/ETH Zürich, Zürich, Switzerland
[3]Viral Immunobiology, Institute of Experimental Immunology, University of Zürich, Zürich, Switzerland
[4]Institute of Medical Genetics and Pathology, University Hospital Basel, Basel, Switzerland

Corresponding author: Obinna Chijioke, Cellular Immunotherapy, Institute of Experimental Immunology, University of Zürich, Winterthurerstrasse 190, 8057 Zürich, Switzerland; Tel: +41 44 635 37 19, Email: chijioke@immunology.uzh.ch

Abstract

Background Humanized tumor models could be particularly valuable for cancer immunotherapy research, as they may better reflect human-specific aspects of the interfaces between tumor and immune system of human cancer. However, endogenous antitumor immunity in humanized models is still largely undefined.

Methods We established a novel autologous humanized mouse tumor model by using NSG mice reconstituted with human immune cells from hematopoietic progenitors and tumors generated from transformed autologous human B cells. We demonstrate growth of solid lymphoid tumors after subcutaneous implantation, infiltration by endogenous human immune cells and immunocompetence of the model.

Findings We found human T cell subsets described in human cancer, including progenitor exhausted (T_{pex}), terminally exhausted ($T_{ex\text{-}term}$) and tissue-resident (T_{RM}) cells in tumor-bearing humanized mice with accumulation of $T_{ex\text{-}term}$ and T_{RM} in the tumor. In addition, we identified tumor-reactive $CD8^+$ T cells through expression of CD137. This subpopulation of de novo arising human $CD137^+$ $CD8^+$ T cells displayed a highly proliferative, fully activated effector and exhausted-like phenotype with enhanced expression of activation and exhaustion markers like PD-1, CD39, CD160, TIM-3, TIGIT and TOX, the senescence marker CD57 (*B3GAT1*) and cytolytic effector molecules such as *PRF1*, *GZMH* and *NKG7*. Moreover, these $CD137^+$ $CD8^+$ T cells exhibited tumor-specific clonal expansion and presented signature overlap with tumor-reactive $CD8^+$ T cells described in human cancer. We demonstrate superior anticancer activity of this exhausted-like human $CD8^+$ T cell subset by adoptive transfer experiments using recipients bearing autologous human tumors. Mice adoptively transferred with $CD137^+$ $CD8^+$ T cells showed reduced tumor growth and higher $CD8^+$ T cell tumor infiltration, correlating with control of human tumors.

Interpretation We established an immunocompetent humanized tumor model, providing a tool for immunotherapy research and defined effective anticancer activity of human effector $CD8^+$ T cells with an exhausted-like phenotype, supporting clinical exploration of such cells in adoptive T cell therapies.

Funding Swiss Cancer Research foundation.

Keywords: Human cancer immunology; Humanized cancer models; Phenotypic markers; T cells; Exhaustion; Adoptive cell therapy

Research in context

Evidence before this study

Antitumor immune responses and outcome of immunotherapeutic interventions are not always consistent between mouse models of cancer and data available in humans. This may be due to species-specific differences, therefore models with a potential for better translatability are needed, such as humanized mouse models. However, there is limited data on human antitumor T cell immunity in humanized mice.

Added value of this study

In this study, we established an immunocompetent humanized tumor model that recapitulates hallmarks of human antitumor T cell responses, offering the possibility for further translational investigation of the interface between human tumors and endogenous anticancer immunity. Furthermore, using functional *in vitro* assays and adoptive transfer, our study demonstrates the key importance of human effector $CD8^+$ T cells with an activated and exhausted-like phenotype in the antitumor immune response.

Implications of all the available evidence

The autologous humanized tumor model provided in this study can serve as a tool to elucidate human-specific immune features. By bridging a gap between syngeneic mouse tumor models and human-specific antitumor immune responses, the model may help open up avenues for greater translatability of preclinical data. Our findings suggest that exhausted-like effector $CD8^+$ T cells can be harnessed for clinical development of adoptive T cell therapies.

Introduction

The characterization of phenotypic traits that can faithfully identify tumor-specific $CD8^+$ T cells with functional anticancer activity is an area of intense research. Recent studies have shown tumor-reactive $CD8^+$ T cells to be rare in patients with various cancers and thus challenging to explore (1,2). Preclinical studies in mice have shown that $CD8^+$ T cells displaying an exhausted-like phenotype have decreased effector function (3). Reinvigoration of exhausted antitumor T cells is thought to be a key component of response to immune checkpoint blockade. Nevertheless, studies in individuals with cancer have correlated exhausted-like phenotypic states of $CD8^+$ T cells with tumor reactivity and clinical benefit (4,5).

Undoubtedly, tumor models using inbred and transgenic mice have contributed substantially to our understanding of tumor immunobiology and have been fundamental to the development of cancer immunotherapies that are now used on a routine basis in the clinic (6,7). However, human clinical studies (8) have shown that the outcome of cancer immunotherapies can significantly diverge from those of mouse models of cancer (9). This might be due to a relative lack of genetic diversity of mouse models compared to humans (10) but also to differences in aspects of gene expression networks (11), genomic organization (12) and tissue structure of the immune system of mice and humans (13). Xenograft mouse models using adoptive transfer of human immune cells rely on immunodeficient hosts, precluding analysis of the impact of endogenous adaptive antitumor immunity. Furthermore, in most preclinical studies investigating novel immunotherapy targets, monoclonal T cells with a single antigen specificity are explored (14,15) while polyclonal T cell responses might be a biomarker for favorable patient outcome to immunotherapy (16) and thus be more informative.

Complementing existing mouse tumor models, the use of mice with reconstituted human immune system components (HIS mice) holds hitherto underexplored translational potential to advance human cancer immunology (17). Yet, endogenous antitumor immunity in these models has remained largely undefined, mainly due to allogeneic reactivity of the reconstituted human T cells against allogeneic tumors (18), making a distinction of alloreactivity from tumor-specific immune responses challenging.

In this study, we demonstrate that reconstitution of human immune system components across independent donors can mount endogenous antitumor T cell responses to autologous human tumor challenge in HIS mice. A polyclonal population of human effector $CD8^+$ T cells with an activated and exhausted-like phenotype that arises de novo in tumor-bearing HIS mice, resembling exhausted tumor-reactive lymphocytes found in patients with cancer, is able to control autologous human tumor growth *in vivo*. Thus, we provide a tool to investigate human antitumor T cell immunity and direct evidence of clinically relevant anticancer activity of expanded human tumor-reactive effector $CD8^+$ T cells with an activated and exhausted-like, non-progenitor-like phenotype.

145 # Methods

146 **HIS & NSG mice**

147 NSG (NOD.Cg-Prkdc<scid>Il2rg<tm1Wjl>/SzJ (#005557)) mice were purchased from The
148 Jackson Laboratory and bred and housed under specific pathogen-free conditions at the
149 Laboratory Animal Services Center (LASC) Zurich, University of Zurich. To generate HIS mice,
150 newborn pups (1-5 days old) were irradiated (1 Gy) and intrahepatically injected with 0.2 x 10^6
151 human $CD34^+$ hematopoietic progenitor cells derived from human fetal liver (Advanced
152 Bioscience Resources, USA). $CD34^+$ cells were isolated by MACS technology (Miltenyi, Cat.
153 130-046-703) following the manufacturer's instructions. At 3 months of age, reconstitution of
154 human immune cells was assessed in PBMC from tail vein blood by flow cytometry (19).
155 Reconstitution analysis included staining for human CD45, CD3, CD4, CD8, CD19, NKp46 and
156 HLA-DR. Only mice with a sufficiently high frequency of human CD45 (>25% of leukocytes)
157 were included in the experiments. Both female and male mice were used in the experiments
158 and no sex-based analysis was performed. All animal experiments were performed according
159 to approved licenses by the veterinary office of the canton of Zurich, Switzerland (ZH049/20
160 and ZH067/2023).

161

162 **LCL generation and tumor model**

163 LCL were generated from $CD19^+$ B cells derived from the same autologous human fetal liver
164 tissue from which the $CD34^+$ cells for reconstitution of the human immune system in the same
165 experiment were derived. $CD19^+$ cells were isolated from the HFL tissue's $CD34^-$ fraction by
166 MACS technology (Miltenyi, Cat. 130-050-301) according to the manufacturer's instructions.
167 0.25 x 10^6 $CD19^+$ human B cells were transformed by infection with Epstein-Barr virus (EBV
168 B95-8; produced as previously described (19)) at an MOI of 0.1 - 0.15 and cultured in RPMI/
169 10% FCS/ 1% Penicillin/ Streptomycin.

170 LCL tumors were injected subcutaneously into the left flank under isoflurane narcosis. For
171 generation and phenotyping of tumor-reactive T cells, 5 x 10^6 autologous LCL tumor cells were
172 resuspended in PBS and right before injection mixed in a 1:1 V/V ratio with Corning® Matrigel®
173 Growth Factor Reduced (GFR) Basement Membrane Matrix (Milian, Cat. 354230).

174 For adoptive cell transfer experiments, 2 x 10^6 LCL were injected s.c. in a 1:1 V/V mix with
175 Matrigel and three days after tumor injection, 2 x 10^6 T cells (HIS recipient mice) or 10 x 10^6
176 (NSG recipient mice) were adoptively transferred by tail vein injection. Tumor size was
177 monitored by calipering (3x/week or daily). Tumor volume was calculated as volume [mm^3] =
178 length [mm] x $width^2$ [mm^2] x 0.52. General health was monitored by weighing and health
179 parameter scoring (3x/week or daily, according to animal license). PBMC composition and
180 expansion of adoptively transferred T cells were monitored by weekly tail vein bleeding and
181 flow cytometric analysis. White blood cell (WBC) counts were measured from blood with an
182 automatic cell counting machine (DxH 500, Beckman Coulter). Animals were euthanized when
183 they met pre-defined termination criteria defined in the animal license.
184

185 **T cell isolation and expansion**

186 Spleens from LCL tumor-bearing and naïve HIS mice were harvested 16-18 days after s.c.
187 tumor injection. Splenocytes were labelled with fluorescently labelled antibodies and sorted by
188 fluorescent activated cell sorting (FACS). $CD137^+$, $CD137^-$ and $CD137^-PD\text{-}1^-$ $CD8^+$ T cells were
189 sorted from tumor-bearing HIS mice and bulk $CD8^+$ T cells were isolated from naïve HIS mice.
190 Sorted T cells were expanded by a rapid expansion protocol (REP), as described elsewhere
191 (20). REP medium consisted of a 1:1 mix of RPMI (Gibco, Cat. 7001612) and X-Vivo (Lonza,
192 Cat. BE02-060F) containing 10% FCS (Biochrome, Cat. S0615-500ML) and 1% Penicillin/
193 Streptomycin (Thermo Fisher, Cat. 7001592). After sorting, T cells were cultured in REP
194 medium with 30 ng/µl OKT3 (Miltenyi, Cat. 130-093-387), 3000 IU/ml IL-2 (Peprotech, Cat.
195 200-02) and a 200-fold excess of irradiated (50 Gy) allogeneic PBMC derived from 3 healthy
196 donors at a total cell density of 5 x 10^6 cells/ml. Starting at day 7, cells were adjusted with REP
197 medium to 0.5-1 x 10^6 cells/ml and fresh IL-2 (3000 IU/ml) was added every second day. Cells
198 were expanded for a total of 14-16 days until use for further experiments.
199

200 **Cell isolation from organs**

201 For reconstitution analysis and weekly bleeding, 100-150 µl of tail vein blood was collected
202 into EDTA tubes (BD Microtainer, BD, Cat. 365975) and erythrocytes were lysed by incubation

203 with lysis buffer. Leukocytes were stained for flow cytometric analysis. For PBMC isolation on
204 the day of sacrifice, blood was harvested by heart puncture and erythrocytes were lysed with
205 erythrocyte lysis buffer. For splenocyte isolation, spleens were removed and meshed through
206 a 70 µm cell strainer in PBS and lymphocytes were isolated by Ficoll-Paque (GE Healthcare,
207 17-5442-03). Single cell suspensions were washed and stained for flow cytometric analysis.
208 For tumor-infiltrating lymphocyte (TIL) isolation, tumors were removed from the flank and skin
209 was removed from the tumors. Tumors were cut into small pieces with scissors and then
210 incubated with digestion mix (DMEM (Life technologies, Cat. 7001566) containing 2% FCS
211 (Biochrome, Cat. S0615-500ML), 1 mg/ml Collagenase IV (Roche, Cat. 7002219), 10ug/ml
212 DNase I (Roche, Cat. 7002221) and 1.2 mM CaCl2; approx. 1.5 ml/tumor, incubation for 45
213 min, 37°C). The tumor digest was diluted with 20 ml RPMI or PBS and meshed over a 70 µm
214 cell strainer. Single cell suspensions were washed and then stained for flow cytometric
215 analysis.
216
217 **Flow cytometry**
218 For surface staining, cells were washed in PBS and stained with an antibody master mix for
219 20 min at 4°C in the dark. For intracellular staining, cells were first stained for surface antigens
220 and fixable live/dead marker, then fixed and permeabilized using the BD Pharmingen™
221 Transcription Factor Buffer Set (BD, Cat. 562574) according to the manufacturer's instructions,
222 then stained for intracellular or intranuclear antigens for 50-60 minutes. Cells were washed in
223 PBS and acquired on a BD LSRFortessa™ or Cytek Aurora.
224 Antibodies for reconstitution analysis of HIS mice (all antibodies are anti-human): CD45-Pacific
225 Blue (Biolegend, HI30, Cat. 304029), CD3-PE (Biolegend, UCHT1, Cat. 300408), CD4-APC-
226 Cy7 (Biolegend, RPA-T4, Cat. 300518), CD8-PerCP (Biolegend, SK1, Cat. 344708), HLA-DR-
227 FITC (Biolegend, L243, Cat. 307604), CD19-PE-Cy7 (Biolegend, HIB19, Cat. 302216),
228 NKp46-APC (BD, 9-E2, Cat. 558051), Zombie Aqua™ Fixable Viability Kit (Biolegend, Cat.
229 423101).
230 Antibodies for flow cytometry-based sorting of T cells: CD3-FITC (Biolegend, UCHT1, Cat.
231 300406), CD4-APC-Cy7 (Biolegend, RPA-T4, Cat. 300518), CD8-BV650 (Biolegend, SK1,

232 Cat. 344730), CD45-Pacific Blue (Biolegend, HI30, Cat. 304029), CD137-APC (Miltenyi,
233 REA765, Cat. 130-110-901), PD-1-PE-Dazzle (Biolegend, EH12.2H7, Cat. 329940), Zombie
234 Aqua™ Fixable Viability Kit (Biolegend, Cat. 423101).
235 Antibodies for phenotyping in Panel 1: CD45-Pacific Blue (Biolegend, HI30, Cat. 304029),
236 CD3-PerCP-Cy5.5 (Biolegend, UCHT1, Cat. 300429), CD4-APC-Cy7 (Biolegend, RPA-T4,
237 Cat. 300518), CD8-BV650 (Biolegend, SK1, Cat. 344730), CD45RA-BV785 (Biolegend,
238 HI100, 304139), CD62L-FITC (BD, DREG-56, Cat. 555543), CD19-PE-Cy7 (Biolegend,
239 HIB19, Cat. 302216), HLA-DR-BV605 (BD, g46-6, Cat. 562845), CD39-BV711 (Biolegend, A1,
240 Cat. 328228), CD69-Alexa Fluor 700 (Biolegend, FN50, Cat. 310921), PD-1-PE-Dazzle
241 (Biolegend, EH12.2H7, Cat. 329940), TCF1-PE (Biolegend, 7F11A10, Cat. 655207), CD137-
242 APC (Miltenyi, REA765, Cat. 130-110-901), Zombie Aqua™ Fixable Viability Kit (Biolegend,
243 Cat. 423101); in Panel 2: CD3-FITC (Biolegend, UCHT1, Cat. 300406), CD4-PE-Cy7
244 (Biolegend, RPA-T4, Cat. 300512), CD8-BV650 (Biolegend, SK1, Cat. 344730), CD45-BV711
245 (Biolegend, HI30, Cat. 304050), CD137-APC-Fire750 (Biolegend, 4B4-1, Cat. 309834),
246 Granzyme B-APC-Alexa700 (Biolegend, QA16A02, Cat. 372222), Ki-67-BV605 (Biolegend,
247 Ki-67, Cat. 350522), PD-1-PE-Dazzle (Biolegend, EH12.2H7, Cat. 329940), Perforin – BV421
248 (Biolegend, dG9, Cat. 308122), TCF1-PE (Biolegend, 7F11A10, Cat. 655207), TOX-APC
249 (Miltenyi, REA473, Cat. 130-118-335), Zombie Aqua™ Fixable Viability Kit (Biolegend, Cat.
250 423101); in Panel 3: CD45-BUV395 (BD, HI30, Cat. 563792), CD3-Pacific Blue (Invitrogen,
251 S4.1, Cat. MHCD0328), CD4-BUV495 (BD, SK3, Cat. 612936), CD8-BUV563 (BD, RPA-T8,
252 Cat. 612914), CD19-PE-Cy5 (Biolegend, HIB19, Cat. 302210), CD45RA-BV785 (Biolegend,
253 HI100, 304139), CD62L-BV605 (Biolegend, DREG-56, Cat. 304834), CD39-PE-Fire810
254 (Biolegend, A1, Cat. 328245), CD69-BUV805 (BD, FN50, Cat. 748763), CD137-APC (Miltenyi,
255 REA765, Cat. 130-110-901), PD-1-PE-Dazzle (Biolegend, EH12.2H7, Cat. 329940), HLA-DR-
256 FITC (Biolegend, LN3, Cat. 327006), TCF1-PE (Biolegend, 7F11A10, Cat. 655207), CD160-
257 PerCP-Cy5.5 (Biolegend, BY55, Cat. 341210), LAG3-BV650 (Biolegend, 11C3C65, Cat.
258 369316), TIM3 – Alexa Fluor 700 (R&D Systems, Clone 344823, Cat. FAB2365N) , Galectin-9
259 -PE-Cy7 (Biolegend, 9M1-3, Cat. 348916), TIGIT-APC-Cy7 (Biolegend, A15153G, Cat.

260 372734), Ki-67-BV510 (Biolegend, Ki-67, Cat. 350518), CD103-BV711 (Biolegend, Ber-ACT8,
261 Cat. 350222), LIVE/DEAD™ Fixable Blue Dead Cell Stain Kit (Invitrogen, Cat. L23105).
262
263 **Co-expression analysis**
264 For co-expression analysis of flow cytometric data, cells were manually gated on live, singlet
265 human $CD8^+$ T cells. Cells were analyzed using CRUSTY webtool (21), where clustering was
266 performed using Phenograph algorithm and default settings for UMAP generation.
267
268 **IFN-γ ELISpot and TNFα ELISA**
269 For IFN-γ ELISpot, ELISpot plates (Merck, Cat.MAIPN4550) were activated with 35% ethanol,
270 washed and coated overnight with anti-IFN-γ coating antibody (mAb-1-D1K, Mabtech, Cat.
271 3420-3-1000). Plates were washed and T cells were co-cultured with autologous LCL in RPMI/
272 10% FCS/ 1% Pen/Strep at an effector: target ratio of 5:1 for 16-24 hours. After incubation,
273 supernatant was harvested, stored at -20°C and used for TNFα ELISA. Wells were washed
274 and incubated for 2 hours with biotinylated anti-IFN-γ detection antibody (mAb-7-B6-1-Biotin,
275 Mabtech, Cat. 3420-6-250). Afterwards, wells were washed and incubated with Streptavidin-
276 ALP (Mabtech, Cat. 3310-10) for 1 hour. Wells were then washed again and spots were
277 developed with filtered substrate solution BCIP/ NBT-plus (Mabtech, Cat. 3650-10). When
278 distinct spots were visible, the plate was washed and dried overnight. Plates were acquired
279 with an ELISpot reader (AID classic, AID GmbH) and spots were automatically counted using
280 AID ELISpot 8.0 software (AID GmbH).
281 TNFα ELISA was performed with the supernatant from T cell and LCL co-culture as described
282 above using the human TNFα $ELISA^{BASIC}$ kit (Mabtech, Cat. 3512-1H-6), following
283 manufacturer's instructions. Plates were acquired using an ELISA reader (infinite M200Pro,
284 Tecan) and analyzed with the i-control 2.0 software (Tecan).
285
286 **Immunohistochemistry**
287 Tumors were fixed in 4% paraformaldehyde and embedded in paraffin. Sample embedding,
288 preparation and staining was performed by the Pathology department of the University Hospital

289 Basel. Slides were acquired on an automated slide scanning brightfield microscope (Vectra 3,
290 Akoya Biosciences) and quantified using InForm software (Akoya Biosciences).
291
292 **Bulk RNAseq and TCR profiling**
293 RNA was extracted from 5 x 10^6 T cells using the RNeasy® Mini Kit (Qiagen, Cat. 74106). RNA
294 extraction was performed following the instructions from the "Purification of Total RNA from
295 Animal Cells Using Spin Technology" protocol given in the RNeasy® Mini Handbook, including
296 homogenization with QIAshredders (Qiagen, Cat. 79654) and on-column DNA digestion with
297 the RNase-free DNase Set (Qiagen, Cat. 79254). All further steps were performed by the
298 Functional Genomics Center Zurich (FGCZ). The quality of the isolated RNA was determined
299 with a Qubit® (1.0) Fluorometer (Life Technologies, California, USA) and a Bioanalyzer 2100
300 (Agilent, Waldbronn, Germany). Only those samples with a 260 nm/280 nm ratio between 1.8–
301 2.1 and a 28S/18S ratio within 1.5–2 were further processed. The TruSeq RNA Sample Prep
302 Kit v2 (Illumina, Inc, California, USA) was used in the succeeding steps. Briefly, total RNA
303 samples (600 ng) were poly A enriched and then reverse-transcribed into double-stranded
304 cDNA. The cDNA samples were fragmented, end-repaired and polyadenylated before ligation
305 of TruSeq adapters containing the index for multiplexing fragments containing TruSeq adapters
306 on both ends were selectively enriched with PCR. The quality and quantity of the enriched
307 libraries were validated using Qubit® (1.0) Fluorometer and the Caliper GX LabChip® GX
308 (Caliper Life Sciences, Inc., USA). The product is a smear with an average fragment size of
309 approximately 260 bp. The libraries were normalized to 10nM in Tris-Cl 10 mM, pH8.5 with
310 0.1% Tween 20. After library quantification, libraries were prepared for loading accordingly to
311 the NovaSeq workflow with the NovaSeq6000 Reagent Kit (Illumina, Catalog
312 No. 20012865). Cluster generation and sequencing were performed on a NovaSeq6000
313 System with a run configuration of single end 100bp. RNA-seq data analysis consisted of the
314 following steps: The raw reads were first cleaned by removing adapter sequences, trimming
315 low quality ends, and filtering reads with low quality (phred quality <20) using Fastp (Version
316 0.20) (22). Sequence pseudo alignment of the resulting high-quality reads to the human
317 reference genome (build GRCh38.p13 and GENCODE gene models release 37) and

quantification of gene level expression was carried out using Kallisto (Version 0.46.1) (23). Differential expression was computed using the generalized linear model implemented in the Bioconductor package DESeq2 (R version: 4.2.2, DESeq2 version: 1.38.1) (24). Genes showing altered expression with adjusted (Benjamini and Hochberg method) p-value < 0.05 were considered differentially expressed. RNA-seq expression data underwent preprocessing to remove duplicated genes. Subsequently, we utilized the CreateSeuratObject() function within the Bioconductor package Seurat (R version: 4.2.2, Seurat version: 5.0.1) (25) to construct a Seurat object, facilitating downstream analyses. Normalization of the expression data was performed using the NormalizeData() function, with experimental group assignments explicitly indicated within the Seurat object. To delineate the gene signatures characterizing distinct T cell phenotypes, we curated pertinent signatures from previous studies. Genes absent in our expression data were systematically filtered out. Next, employing the AddModuleScore() function, we computed module scores for each gene signature across experimental groups and values were scaled for heatmap visualization. For the TCR analysis the read alignment to the Human genome was performed with STAR (v2.7.10b) (26). TCR sequences (CDR3 of TRA, TRB, TRG and TRD) were reconstructed from bulk RNAseq data using TRUST4 (v1.0.10) (27). Out-of-frame sequences were excluded from the analysis. TCR repertoire analysis was performed using the R package Immunarch (28).

Statistics

Statistical analysis was performed using Prism 10 Software (GraphPad Software, Inc). Figure legends indicate which statistical test was performed.

Study approval

Animal experiments were conducted according to licenses approved by the veterinary office of the canton of Zurich, Switzerland (ZH049/20 and ZH067/2023).

BioRender

Schematics were generated with a licensed version of BioRender.

Author contributions

Conceptualization, J.M. and O.C.; Methodology, J.M., M.K. and O.C.; Investigation, J.M., M.K., L.E., L.O. and O.C.; Writing – Original Draft: , J.M. and O.C.; Writing – Review & Editing, , J.M. C.M. and O.C.; Funding Acquisition, O.C.; Resources, L.O. and C.M.; Supervision, O.C.

Declaration of Interests

The authors declare that they have no competing interests.

Acknowledgments

We would like to thank Fernando Canale for help with gene signature analysis and Daniel E. Speiser for critically reading the manuscript. Funding: This research was supported by Swiss Cancer Research foundation (KFS-5292-02-2021 to O.C.).

Data Sharing

Supplemental data are provided with this paper. All data are also available upon request.

376 # Results

377 **Establishment of an autologous HIS mouse tumor model**

378 We established and characterized a novel tumor model in which immunocompetent,
379 humanized mice are subcutaneously implanted with autologous human tumor cells. For this
380 aim, we isolated $CD34^+$ hematopoietic progenitor cells (HPC) and $CD19^+$ B cells from the same
381 human HPC donor tissue. $CD34^+$ HPCs were engrafted into NSG mice to reconstitute
382 components of the human immune system (from here on referred to as human immune system
383 (HIS) mice), while $CD19^+$ B cells were transformed into lymphoblastoid cell lines (LCL) by
384 infection with the oncogenic Epstein-Barr virus (EBV) (**Figure 1A**).

385 To characterize LCL tumorigenicity and tumor growth in the presence or absence of an
386 autologous human immune system, HIS mice reconstituted with HPCs autologous to the tumor
387 or NSG mice were injected subcutaneously with LCLs. In both recipient strains, palpable
388 tumors formed at the site of implantation. In HIS mice, in the presence of an endogenous
389 immune system, tumors showed progressive growth until approximately day 18 and
390 subsequently, a majority of tumors showed regression (**Figure 1B**). In contrast, in NSG mice
391 without an endogenous immune system, tumors increased in size until termination criteria were
392 reached (**Figure 1C**). These data suggested a functional antitumor response mediated by
393 components of the reconstituted human immune system, i.e. immunocompetence, in our
394 autologous HIS mouse tumor model.

395

396 **Endogenous antitumor immune response in HIS mice**

397 To investigate the tumor regression that we observed in the presence of an autologous human
398 immune system, we next characterized the immune response in tumor-bearing HIS mice.
399 Around the same time of tumor regression, we found weight loss in HIS mice (**Figure 1D**), but
400 not in tumor-bearing NSG mice (**Figure 1E**). This indicated immunopathology related to the
401 endogenous human antitumor immune response, reminiscent of cancer cachexia (29) rather
402 than an effect of tumor growth per se. Additionally, we found increases in spleen-to-body weight
403 ratio, total splenocyte count and white blood cell count in tumor-bearing HIS mice (**Figure 1,**
404 **F-H**), suggesting immune cell proliferation occurring in response to tumor growth. Furthermore,

405 tumors in HIS mice showed infiltration by endogenous human immune cells, including $CD8^+$ T
406 cells (Supplemental Figure 1).

407 The frequency of human $CD3^+$ T cells in tumor-bearing HIS mice in spleen (**Figure 2A**)
408 and circulation (Supplemental Figure 2A) increased significantly compared to naïve HIS mice.
409 Moreover, tumor-bearing HIS mice showed an increased frequency of $CD8^+$ T cells, suggesting
410 preferential expansion (**Figure 2A** and Supplemental Figure 2A). These $CD8^+$ T cells exhibited
411 differentiation towards an effector memory (T_{EM}) phenotype and, to a lower degree, central
412 memory (T_{CM}) phenotype, whereas non-tumor bearing HIS mice had higher frequencies of
413 naïve T cells ($T_{naïve}$) (**Figure 2B** and Supplemental Figure 2B). Consistent with an exhausted
414 effector-like phenotype, $CD8^+$ T cells from tumor-bearing HIS mice also showed enhanced
415 expression of the exhaustion/activation markers PD-1, CD39 and HLA-DR (**Figure 2C** and
416 Supplemental Figure 2C) as well as trending towards increased TOX expression (**Figure 2D**
417 and Supplemental Figure 2D), while exhibiting significantly reduced levels of the
418 progenitor/stemness-related marker TCF1 (30) (**Figure 2D** and Supplemental Figure 2D).

419 Similar to the increased $CD8^+$ T cell frequencies in secondary lymphoid tissue (spleen)
420 and circulation, tumors in HIS mice exhibited predominant infiltration by $CD8^+$ T cells (**Figure**
421 **2E** and Supplemental Figure 1C). The majority of autologous tumor-infiltrating human $CD8^+$ T
422 cells had a T_{EM}-like phenotype, with a lower proportion of T_{CM} and greatly reduced proportions
423 of T_{EMRA} and naïve T cells (**Figure 2F**). Tumor-infiltrating $CD8^+$ T cells displayed high
424 expression of exhaustion and activation markers PD-1 (91.0%±12.1), CD39 (56.4%±22.8) and
425 HLA-DR (53.9%±22.4) (**Figure 2G**), low levels of TCF1 (5.6%±5.0) (**Figure 2H**), while a
426 fraction of tumor-infiltrating $CD8^+$ T cells expressed TOX (21.7%±14.81) (**Figure 2H**).
427 Dimensionality reduction by UMAP revealed obvious differences of $CD8^+$ T cell landscapes
428 between tumor-infiltrating lymphocytes (TIL) and spleen (**Figure 2I**). Together, the phenotype
429 of human $CD8^+$ T cells in tumor-bearing HIS mice was reminiscent of $CD8^+$ T cell phenotypes
430 described in human cancer (31,32).

431 Progenitor exhausted T cells (T_{pex}; $TCF1^+PD\text{-}1^+$) play an important role for immunotherapy
432 of human cancer. T_{pex} have been described as precursors of exhausted cytotoxic T cells (T_{ex};
433 $TCF1^-PD\text{-}1^{+,}$, further subdivided into $TCF1^-PD\text{-}1^+CD69^-$ intermediate exhausted ($T_{ex\text{-}int}$) and

434 TCF1$^-$PD-1$^+$CD69$^+$ terminally exhausted ($T_{ex\text{-}term}$) T cells (33)), which exhibit effector function
435 but reduced self-renewal and long-term survival, making T_{pex} cells an important reservoir of
436 antitumor T cells (33–35). Interestingly, we detected an increased fraction of CD8$^+$ T_{pex} cells in
437 secondary lymphoid tissue (spleen) of tumor-bearing HIS mice compared with tumor (**Figure**
438 **2J**). This distribution recapitulates human cancers, where a higher frequency of T_{pex} is found
439 in lymph nodes compared to the tumor site (34). In addition, we found a significantly higher
440 proportion of terminally exhausted CD8$^+$ T cells ($T_{ex\text{-}term}$; TCF1$^-$PD-1$^+$CD69$^+$) within the tumor
441 compared to the spleen, a secondary lymphoid organ (**Figure 2J**), again consistent with what
442 has been described in human cancer (34,35).

443 Tissue-resident-memory (T_{RM}) T cells (CD69$^+$CD103$^+$) within tumors are another T cell
444 subset of interest for immunotherapy research. The presence of T_{RM} cells has been associated
445 with a favorable outcome in certain cancer types and based on their expression of immune
446 checkpoint molecules, tumor-reactive T_{RM} cells also constitute a target for immune checkpoint
447 blockade (36). We detected T_{RM}-like (CD69$^+$CD103$^+$) CD8$^+$ T cells in tumor-bearing HIS mice
448 and found a significantly higher abundance in tumor compared with spleen (**Figure 2K**).

449 The presence and identification of these human CD8$^+$ T cell subsets, which are considered
450 relevant in human cancer and are thought to play critical roles in response to immunotherapy,
451 underscores the translational value of our humanized mouse model for immunotherapy
452 research.

453

454 **Activated and exhausted-like, cytotoxic effector-like phenotype of human CD137$^+$ CD8$^+$**
455 **T cells**

456 In human cancers, CD137 has been described as a marker for tumor-reactive T cells (37–39).
457 We similarly identified a population of human CD137$^+$ T cells in tumor-bearing mice (**Figure**
458 **2L**) and characterized the CD8$^+$ T cell population further. Likewise, PD-1 has been reported to
459 be a marker of tumor-reactive T cells in human cancers, both in circulation and within tumor-
460 infiltrating lymphocytes (20,40,41). We observed that of splenic CD8$^+$ T cells from tumor-
461 bearing HIS mice, only a small proportion (10.9%±11.2) were CD137 positive, whereas the
462 majority of CD8$^+$ T cells (83.5%±12.1) expressed PD-1 on their surface (**Figure 2M**). Though

463 there was a small but still significant difference between the overall high level of PD-1
464 expression on CD137$^+$ CD8$^+$ and CD137$^-$ CD8$^+$ T cells from tumor-bearing HIS mice, both these
465 populations expressed PD-1 significantly more than bulk CD8$^+$ T cells from naïve HIS mice
466 (**Figure 2N**). These data suggested that CD137 alone might not be sufficient to delineate
467 tumor-reactive T cell subsets. We therefore included a CD8$^+$ T cell subset negative for both
468 CD137 and PD-1 in our analysis to further explore and distinguish bona fide tumor-reactive
469 from bystander CD8$^+$ T cells in tumor-bearing HIS mice.
470 Indeed, compared to double negative CD137$^-$PD-1$^-$ CD8$^+$ T cells, CD137$^+$ CD8$^+$ T cells and
471 CD137$^-$ CD8$^+$ T cells displayed a T_{EM}-like phenotype, while the double negative CD137$^-$PD-1$^-$
472 population was enriched in naïve-like T cells (Supplemental Figure 2E). Within the splenic
473 CD137$^+$ CD8$^+$ T cell population, we found the highest expression of the exhaustion marker
474 CD39, which has been described as a marker of CD8$^+$ T cells with enhanced tumor reactivity
475 across different human cancers (1,42–46), the activation marker HLA-DR as well as the
476 activation and residency-related marker CD69 (47), while this cell subset also had the
477 strongest expression levels of Ki-67, indicating high proliferation (**Figure 2O** and Supplemental
478 Figure 2F). Additionally, within the CD137$^+$ CD8$^+$ T cell population, we observed significantly
479 increased expression of TOX, a transcription factor associated with exhaustion (48) and
480 drastically reduced levels of the progenitor/stemness-related transcriptional regulator TCF1
481 (30) (**Figure 2O** and Supplemental Figure 2G). Several makers related to T cell exhaustion
482 and activation (49,50) (TIGIT, TIM3, CD160, Galectin-9) were similarly upregulated on CD137$^+$
483 CD8$^+$ T cells (**Figure 2O** and Supplemental Figure 2H). Finally, CD137$^+$ CD8$^+$ T cells displayed
484 the highest levels of the cytolytic molecules granzyme B and perforin compared with CD137$^-$
485 CD8$^+$ T cells or CD137$^-$PD-1$^-$ CD8$^+$ T cells from tumor-bearing HIS mice (**Figure 2O** and
486 Supplemental Figure 2I).
487 The CD137$^+$ CD8$^+$ T cell population contained a significantly higher proportion of $T_{ex\text{-}term}$
488 cells in both spleen and tumor and a significantly lower frequency of T_{pex} in the tumor relative
489 to the CD137$^-$ CD8$^+$ T cell population (Supplemental Figure 2J and 2K). As CD69 is expressed
490 on subsets of both exhausted as well as T_{RM}-like T cells (33), we quantified CD8$^+$ T_{RM}-like
491 (CD69$^+$CD103$^+$) T cells and found no difference between CD137$^+$ and CD137$^-$ T cells in the

492 spleen (Supplemental Figure 2L). In the tumor, where an overall higher proportion of T_{RM}-like
493 T cells was present compared to spleen (**Figure 2K**), the CD137$^+$ CD8$^+$ T cell population
494 contained significantly fewer T_{RM}-like T cells compared to CD137$^-$ CD8$^+$ T cells (Supplemental
495 Figure 2M). Thus, the majority of CD137$^+$ CD8$^+$ T cells did not exhibit a T_{RM}-like phenotype, but
496 consisted of more $T_{ex\text{-}term}$ cells relative to CD137$^-$ CD8$^+$ T cells with only a minor proportion of
497 T_{pex} cells.

498 Analysis of CD8$^+$ T cell clusters (Supplemental Figure 3A) from spleen and tumor
499 demonstrated that CD137 expressing clusters 2, 7 and 10 (Supplemental Figure 3, B and C)
500 co-expressed a large number of markers related to activation/exhaustion (TIGIT, TIM3, PD-1,
501 CD39, CD160). CD8$^+$ T cells in cluster 7, the majority of which was localized in the tumor
502 (Supplemental Figure 3B), additionally expressed LAG-3 (Supplemental Figure 3C). Moreover,
503 co-expression analysis confirmed the presence of a T_{pex}-like cluster (TCF1$^+$PD1$^+$CD69$^-$), which
504 was preferentially found in the spleen (cluster 3). Also, a T_{RM}-like cluster (CD69$^+$CD103$^+$) was
505 detected, which was preferentially found in tumor (cluster 5) (Supplemental Figure 3C).

506 Altogether, de novo arising highly proliferative CD137$^+$ CD8$^+$ T cells exhibited an activated
507 and exhausted-like, cytotoxic effector and least stem-like phenotype relative to the other
508 human CD8$^+$ T cell populations we identified in tumor-bearing HIS mice.

509

510 **Maintained expansion capacity and enrichment of *in vitro* tumor reactivity within an**
511 **activated and exhausted-like human CD8$^+$ T cell subset**

512 To investigate tumor reactivity of CD137$^+$ CD8$^+$ T cells relative to the other T cell subsets,
513 splenic T cells were expanded *ex vivo* (**Figure 3A**). Using a rapid expansion protocol (20), we
514 observed an average expansion of >1000-fold after 14 days for all subsets. Interestingly,
515 although terminally exhausted CD8$^+$ T cells have generally been thought to contain reduced
516 proliferative potential (51), there were no significant differences in the expansion capacity of
517 CD137$^+$ CD8$^+$ T cells displaying the most exhausted-like, $T_{ex\text{-}term}$ enriched phenotype (Figure
518 2O and Supplemental Figure 2, J and K) compared to the other CD8$^+$ T cell populations from
519 tumor-bearing HIS mice or bulk CD8$^+$ T cells from naïve HIS mice (**Figure 3B**). All of the *ex*
520 *vivo* expanded T cell subsets from tumor-bearing HIS mice exhibited differentiation biased to

521 an effector memory-like phenotype (**Figure 3C**). While prior to *ex-vivo* expansion both PD-1
522 and CD39 were strongly increased in CD137$^+$ CD8$^+$ T cells (Figure 2, O and N), both markers
523 were no longer significantly upregulated after expansion. In contrast, HLA-DR remained
524 upregulated on CD137$^+$ CD8$^+$ T cells relative to CD137$^-$PD1$^-$ CD8$^+$ and bulk CD8$^+$ T cells from
525 naïve mice (**Figure 3D**).

526 After co-culture with autologous tumor cells, expanded CD137$^+$ CD8$^+$ T cells showed the
527 highest IFN-γ production by ELISpot, which gradually decreased from CD137$^-$ CD8$^+$ T cells to
528 CD137$^-$PD-1$^-$ CD8$^+$ T cells (**Figure 3E**). Similarly, TNFα secretion was highest in supernatants
529 containing CD137$^+$ CD8$^+$ T cells after co-culture with autologous tumor cells and lowest in
530 CD137$^-$PD-1$^-$ CD8$^+$ T cells (**Figure 3F**).

531 Together, these data indicated enrichment of tumor recognition within CD137$^+$ CD8$^+$ T cells
532 that maintained *ex vivo* proliferative potential, while double negative CD137$^-$PD-1$^-$ CD8$^+$ T cells
533 behaved as bystander cells.

534

535 **Transcriptome analysis reveals tumor-reactive signature in CD137$^+$ CD8$^+$ T cells**

536 To gain insight into differentially expressed genes (DEG) in tumor-reactive CD137$^+$ CD8$^+$ T
537 cells versus CD137$^-$ CD8$^+$ T cells and bystander CD137$^-$PD-1$^-$ CD8$^+$ T cells as well as bulk
538 CD8$^+$ T cells from naïve HIS mice, whole transcriptome RNA sequencing of *ex vivo* expanded
539 T cell subsets was performed. We found a higher number of DEG for the tumor-reactive
540 (CD137$^+$) gene set versus bystander CD8$^+$ T cells from tumor-bearing HIS mice (200 DEG)
541 and versus bulk CD8$^+$ T cells from naïve HIS mice (300 DEG) in comparison to the number of
542 DEG we found for the comparison against CD137$^-$ CD8$^+$ T cells (53 DEG) (**Figure 4A**), the
543 subset with the second highest tumor reactivity *in vitro* (Figure 3, D and E). Principal
544 component analysis (PCA) was consistent with functional data of tumor-specific cytokine
545 production (Figure 3, D and E), showing that the 4 subsets clustered in a gradual way from
546 tumor-reactive (CD137$^+$) to less tumor-reactive (CD137$^-$) and bystander (CD137$^-$PD-1$^-$) CD8$^+$
547 T cells and finally to bulk CD8$^+$ T cells from naïve HIS mice, with the biggest overlap between
548 CD137$^-$PD-1$^-$ bystander CD8$^+$ T cells and bulk human CD8$^+$ T cells from naïve HIS mice
549 (**Figure 4B**).

550 The transcriptomic profile that we found in tumor-reactive CD137$^+$ CD8$^+$ T cells suggested
551 an exhausted/activated-like phenotype with increased expression of *TNFRSF9*, *LAG3*,
552 *PDCD1, TIGIT* and *HLA-DPA1/HLA-DQA1* (**Figure 4, C, E and F**). We also observed
553 enhanced expression of effector molecules associated with cytotoxicity (*GZMH, NKG7* and
554 *PRF1*) as well as *IFNG* (**Figure 4, C, E and F**). Expression of the naïve or stem-like genes
555 *CCR7*, *LEF1* and *BACH2* were diminished (**Figure 4, D-F**) while the senescence marker CD57
556 (52) (*B3GAT1*) and the transcription factor *EOMES* showed the highest transcript level in the
557 CD137$^+$ subset (**Figure 4, C and F**). Although EOMES has been shown to be involved in T cell
558 exhaustion, it has also been reported to be commonly co-expressed with effector molecules in
559 effector T cells and to be essential for anticancer T cell function (53,54).

560 Among upregulated Gene Ontology (GO) terms comparing tumor-reactive CD137$^+$ CD8$^+$
561 T cells against the other three populations, we found the terms interferon-gamma mediated
562 signaling (GO:0060333), antigen processing and presentation (GO:0019882), antigen
563 processing and presentation of peptide or polysaccharide antigen via MHC class II
564 (GO:0002504), immune response (GO:0006955) and adaptive immune response
565 (GO:0002250) (**Figure 4G**). Upregulation of these pathways in the CD137$^+$ population
566 indicated stronger T cell activation and response in comparison to the other populations.

567 To determine T cell states after *ex vivo* expansion, we compared our transcriptome data
568 to published datasets of different T cell states from human cancers (31,46,55–59). A high
569 overlap of signatures originally found in tumor-specific CD8$^+$ T cells from human cancers
570 describing terminally exhausted, exhausted, activated, and progenitor exhausted T cell states
571 was found for CD137$^+$ CD8$^+$ T cells (**Figure 4H**). Overlap with these different signatures might
572 hint to a degree of heterogeneity within the CD137$^+$ CD8$^+$ T cell population after *ex vivo*
573 expansion but confirmed the overall activated/exhausted-like state of these cells that we
574 already observed before *ex vivo* expansion. Signatures for tissue-resident memory and CD8$^+$
575 stem-like memory were downregulated in the CD137$^+$ CD8$^+$ population. Strikingly, comparing
576 tumor-reactive CD137$^+$ CD8$^+$ T cells to bystander CD137$^-$PD-1$^-$ CD8$^+$ T cells or bulk CD8$^+$ T
577 cells from naïve HIS mice, gene sets that have been described to define tumor-reactive T cells
578 in patients with cancer were significantly upregulated ('MANA TIL' (58), 'tumor specific' (56))

579 (**Figure 4I**). These results suggested that the antitumor T cell response in autologous tumor-
580 bearing HIS mice mirrors relevant aspects of the T cell response in cancer patients, thus further
581 supporting the potential translational value of our model.
582
583 **Correlation of clonal expansion with effector function**
584 As another surrogate for tumor recognition, we analyzed clonality of the $CD8^+$ T cell receptor
585 (TCR) repertoire, anticipating tumor-reactive $CD8^+$ T cells would have higher clonal expansion
586 and thus lower diversity than bystander $CD8^+$ T cells. Indeed, we found the total number of
587 clonotypes tending to be the smallest in the tumor-reactive $CD137^+$ subset, and to gradually
588 increase from the less tumor-reactive $CD137^-$ subset to $CD137^-PD\text{-}1^-$ bystander $CD8^+$ T cells
589 to bulk $CD8^+$ T cells from naïve HIS mice (**Figure 5A**), following the gradient of tumor
590 recognition we observed by tumor-specific cytokine production *in vitro* (Figure 3, D and E).
591 Likewise, the estimated sample diversity for the tumor-reactive $CD137^+$ subset was lower than
592 for the other populations (**Figure 5B** and Supplemental Figure 4A). In line with this, the $CD137^+$
593 population had a reduced abundance of rare or very small clonotypes (**Figure 5C** and
594 Supplemental Figure 4, B and C). Conversely, tumor-reactive $CD137^+$ $CD8^+$ T cells from tumor-
595 bearing HIS mice demonstrated a significantly higher abundance of hyperexpanded clones
596 (**Figure 5D**) with the 20 biggest clones occupying a significantly larger repertoire space than
597 in the other populations, suggesting polyclonal expansion (Supplemental Figure 4B).
598 To track the overlap of clonotypes between individual experiments (i.e. donor dependency)
599 and populations, we next performed TCR repertoire overlap analysis (**Figure 5E**). We found
600 that the tumor-reactive $CD137^+$ population showed the biggest overlap with the $CD137^-$ subset
601 and only to a minor extend an overlap with $CD137^-PD\text{-}1^-$ bystander $CD8^+$ T cells or bulk $CD8^+$
602 T cells from naïve HIS mice (**Figure 5, E and G**). Also, analyzing the repertoire of the bulk
603 naïve $CD8^+$ T cell population for each experiment by cross-comparing to each population from
604 each experiment, the overlap with the $CD137^+$ population was significantly less than the
605 overlap with every other population (**Fig. 5F**). These findings suggested that clonotypes arising
606 due to the conditions of expansion were less present in the $CD137^+$ population and that other,
607 presumably tumor-reactive, clonotypes expanded.

608 In addition, we observed that the expansion of individual bona fide tumor-reactive
609 clonotypes was highly donor specific. When comparing the 10 most abundant clonotypes of
610 the CD137$^+$ population per experiment (i.e. per donor), almost no overlap with the CD137$^+$
611 TCR repertoire of any other experiment was detected (**Figure 5G** and Supplemental Figure
612 4D). Finally, to explore an association of clonal expansion with functionality, we correlated the
613 abundance of the top 10 bona fide tumor-reactive clonotypes of the CD137$^+$ population with *in*
614 *vitro* tumor reactivity and found a highly significant correlation of clone size abundance and
615 tumor-specific IFN-γ production by CD8$^+$ T cells (**Figure 5H**). Overall, these data indicated that
616 CD137$^+$ CD8$^+$ T cells derived from tumor-bearing HIS mice expanded polyclonally in a human
617 donor- and tumor-specific manner.
618

619 **Human CD8$^+$ T cells with an activated and exhausted-like phenotype reduce tumor**
620 **growth *in vivo***

621 We next performed adoptive cell transfer (ACT) experiments of *ex vivo* expanded CD8$^+$ T cells
622 in NSG mice previously engrafted with autologous tumors (**Figure 6A**). We initially selected
623 NSG mice as recipients to unambiguously track the transferred T cells and to be able to
624 distinguish their anticancer activity from the endogenous antitumor T cell response in HIS mice.
625 In NSG mice, only ACT with expanded CD137$^+$ CD8$^+$ T cells resulted in reduced tumor growth
626 in a substantial number of recipients, while transfer of bystander CD8$^+$ T cells from tumor-
627 bearing HIS mice or bulk CD8$^+$ T cells from naïve HIS mice did not (**Figure 6, B-D**). Specifically,
628 adoptive transfer of human CD137$^+$ CD8$^+$ T cells from tumor-bearing HIS donors resulted in a
629 partial response (≥30% tumor reduction compared to 'tumor only' group) in almost half of
630 recipients (6 out of 13 tumor-bearing NSG recipients, 46%), while this was observed in only
631 13% of NSG mice treated with CD137$^-$PD-1$^-$ CD8$^+$ T cells from tumor-bearing HIS mice (1/8)
632 and no such response (0%) was seen in NSG recipients of bulk CD8$^+$ T cells from naïve HIS
633 mice (0/6) (**Figure 6D**).

634 Furthermore, a higher frequency of T cells was found in tumor (**Figure 6, E and F**), blood
635 (Supplemental Figure 5A) and spleen (Supplemental Figure 5B) of tumor-bearing NSG mice
636 receiving CD137$^+$ CD8$^+$ T cells compared to recipients transferred with any of the other cell

637 populations. Flow cytometric analysis of tumor-infiltrating lymphocytes (TIL) revealed high
638 $CD3^+$ T cell frequencies (53.65%±21.94) after ACT of expanded $CD137^+$ $CD8^+$ T cells, but only
639 11.64%±11.0 after transfer of bystander $CD8^+$ T cells and 7.25%±5.38 after transfer of bulk
640 $CD8^+$ T cells from naïve HIS mice (**Figure 6E**). Likewise, immunohistochemistry of tumors of
641 NSG mice confirmed T cell infiltration selectively after ACT with $CD137^+$ $CD8^+$ T cells (**Figure**
642 **6F**).

643 Interestingly, while infusion products mainly contained a mix of T_{EM}-like and T_{EMRA} $CD8^+$ T
644 cells (Figure 3C), almost exclusively T_{EM}-like cells were recovered from blood (Supplemental
645 Figure 5C), spleen (Supplemental Figure 5D) and TIL (Supplemental Figure 5E) of recipient
646 NSG mice. Of note, whereas PD-1 was highly expressed on splenic $CD137^+$ $CD8^+$ T cells in
647 tumor-bearing HIS mice (96.49%±3.1) (Figure 2N), PD-1 expression on this population
648 decreased during antigen-independent *ex vivo* expansion (32.45%±29.17) (Supplemental
649 Figure 5F). However, after adoptive transfer of expanded $CD137^+$ $CD8^+$ T cells into tumor-
650 bearing NSG mice, PD-1 expression among $CD8^+$ T cells increased again and was significantly
651 higher in TIL (96.7%±3.65) (**Figure 6G**), blood (Supplemental Figure 5G) and spleen
652 (Supplemental Figure 5H) compared to NSG mice transferred with bystander $CD8^+$ T cells or
653 bulk $CD8^+$ T cells. Apart from the superior tumor control, these data further indicated
654 enrichment of tumor reactivity within $CD137^+$ $CD8^+$ T cells, with very high PD-1 expression
655 serving as a potential marker for productive tumor recognition, but not loss of effector function.
656 As another index of the anticancer activity of $CD137^+$ $CD8^+$ T cells, the degree of tumor
657 infiltration with $CD8^+$ T cells after ACT was inversely correlated with tumor size (**Figure 6H**).
658 Thus, the higher frequency of $CD8^+$ T cells in tumors was likely driven by increased tumor
659 recognition of transferred $CD137^+$ $CD8^+$ T cells, and these cells mediated tumor cell killing.

660 Lastly, ACT of tumor-reactive T cells into autologous tumor-bearing HIS recipient mice
661 (**Figure 6I**) presented an opportunity to model polyclonal TIL transfer therapy in cancer patients
662 (60) in an immunocompetent humanized tumor setting. As observed with NSG recipients,
663 transfer of polyclonal tumor-reactive $CD137^+$ $CD8^+$ T cells into autologous tumor-bearing HIS
664 recipient mice reduced tumor growth (**Figure 6, J-L**). A partial response (≥30% tumor reduction
665 compared to 'tumor only' group) was observed in 77% of HIS mice (10/13) receiving adoptive

transfer of autologous human CD137$^+$ CD8$^+$ T cell derived from tumor-bearing HIS donors, while no such response (0%) was observed in any of the HIS mice (0/9) adoptively transferred with autologous CD137$^-$ or CD137$^-$PD-1$^-$ CD8$^+$ T cells derived from tumor-bearing HIS donors (**Figure 6L**). Importantly, this was achieved without prior conditioning of HIS recipient mice or cytokine support, and the number of transferred tumor-reactive CD137$^+$ CD8$^+$ T cells was fivefold lower compared with transfer in NSG recipients. These data established superior anticancer activity of CD137$^+$ CD8$^+$ T cells with an activated and exhausted-like phenotype in the most complete humanized setting.

Altogether, these adoptive transfer experiments confirmed anticancer activity of human CD137$^+$ CD8$^+$ T cells that developed in autologous tumor-bearing HIS mice, suggesting that our model captured relevant aspects of the immunobiology of human antitumor T cell responses.

695 ## Discussion

696 Using in-depth phenotypic analyses, we established the presence of major, widely recognized
697 human $CD8^+$ T cell subsets known to be important in tumor immunology, like progenitor
698 exhausted (T_{pex}; $TCF1^+PD\text{-}1^+$), terminally exhausted ($T_{ex\text{-}term}$; $TCF1^-PD\text{-}1^+CD69^+$) or tissue
699 resident-like (T_{RM}; $CD69^+CD103^+$) T cells in our autologous humanized tumor model.
700 Interestingly, we found $CD8^+$ T_{pex} cells to be more abundant in secondary lymphoid tissue
701 (spleen) compared to tumor and vice versa $CD8^+$ $T_{ex\text{-}term}$ cells to be more abundant in tumor
702 compared to spleen. This seems consistent with the mechanisms of formation of antitumor
703 immunity as currently understood (61). Likewise, tissue-resident-like (T_{RM}) T cells were
704 enriched in the tumor relative to spleen, as would be expected. Furthermore, we identified a
705 proliferative human $CD8^+$ T cell subset in tumor-bearing HIS mice that expressed activation
706 and exhaustion markers including very high levels of PD-1 and CD39 while having low
707 expression of the progenitor marker TCF1 but high expression of TOX. This $CD137^+$ $CD8^+$ T
708 cell subset, while being $PD\text{-}1^{hi}CD39^+$, displayed increased abundance of a $T_{ex\text{-}term}$ phenotype
709 with co-expression of inhibitory receptors like TIM-3, TIGIT, CD160 and galectin-9. At the same
710 time, $CD137^+$ $CD8^+$ T cell contained fewer T_{RM}-like cells, which was reflected by a relative lack
711 of a tissue-resident signature even after expansion. However, we note that the expansion,
712 which was necessary to achieve the cell numbers required for adoptive transfer, may have led
713 to some alteration of populations, as evidenced, for example, in the downregulation of PD-1
714 and CD39 on the protein level after expansion. Nevertheless, most activation and exhaustion
715 markers were still increased on the transcript level in expanded $CD137^+$ $CD8^+$ T cells relative
716 to the other populations. Furthermore, expanded $CD137^+$ $CD8^+$ T cells from tumor-bearing HIS
717 mice showed enrichment in gene signatures of exhaustion. Functionally, $CD137^+$ $CD8^+$ T cells
718 exhibited increased tumor reactivity as demonstrated by enhanced cytokine production after
719 coculture with autologous tumor cells. Importantly, by means of adoptive transfer, we uniquely
720 provide direct *in vivo* evidence of superior anticancer activity of these human tumor-reactive
721 effector $CD8^+$ T cells displaying an activated and exhausted-like phenotypic state.

722 We have leveraged this human $CD8^+$ T cell subset arising de novo in tumor-bearing HIS
723 mice for transcriptomic analysis and TCR profiling to demonstrate across donors overlap with

724 tumor-reactive CD8$^+$ T cell signatures from human cancers (56,58) as well as tumor-induced
725 polyclonal expansion. Polyclonality of neoantigen-specific CD8$^+$ T cells in blood and tumor has
726 recently been shown to be associated with response to PD-1 immunotherapy in patients with
727 melanoma (16). Congruence of our model data across donors with these clinical benchmarks
728 suggests robustness and translational validity of our findings.

729 Of note, CD39$^+$CD8$^+$ T cells expressing high levels of PD-1 have been described to be
730 enriched for tumor reactivity and clonal proliferation, predicting efficacy of immunotherapy in
731 human lung cancer (46). Likewise, the abundance of intratumoral CD39$^+$CD8$^+$ T cells
732 displaying upregulated exhaustion markers has been shown to be prognostic for improved
733 progression-free and overall survival in individuals with treatment-naïve early stage lung
734 cancer (62). Furthermore, PD-1^{hi}CD39$^+$ CD8$^+$ T cells correlated with improved survival in
735 patients with endometrial cancer (45) and the signature of similar CD8$^+$ T cells with increased
736 TOX expression predicted survival in patients with breast cancer (44). Recently, pre-existing
737 exhausted-like tumor-reactive CD8$^+$ T cells have been associated with favorable outcome to
738 immunotherapy in head and neck cancer (63). On the other hand, higher abundance of TCF1$^+$
739 stem-like CD8$^+$ T cells with a CD39$^-$CD69$^-$ phenotype in TIL products was associated with
740 better response after TIL transfer in patients with melanoma (64). However, by single-cell
741 analysis of lung tumors, this phenotype could not be identified in neoantigen-reactive T cells
742 (65). While we have not addressed and thus cannot exclude a contribution of the minor TCF1$^+$
743 fraction within the human tumor-reactive CD8$^+$ T cells in our model, our data emphasize the
744 key importance of exhausted-like effector CD8$^+$ T cells in the antitumor immune response.

745 The striking phenotypic similarity of tumor-reactive CD8$^+$ T cells that have been shown to
746 correlate with clinical benefit and the polyclonally expanded human tumor-reactive CD8$^+$ T cell
747 cells from tumor-bearing HIS mice that we demonstrated to possess superior *in vivo* anticancer
748 activity highlights the translational potential of our model. Hence, the novel immunocompetent
749 human tumor model that we developed using HIS mice with human immune cells reconstituted
750 from hematopoietic progenitor cells that are autologous to tumor might bridge a gap between
751 syngeneic mouse tumor models and human-specific antitumor immune responses (13,66). Our
752 model demonstrates hallmarks of human antitumor T cell responses and thus may provide a

753 tool that should allow further investigation of drivers of anticancer activity in human $CD8^+$ T
754 cells in cancer immunotherapy research. Overall, the endogenous human immune system in
755 HIS mice markedly influenced tumor and host, allowing for experimental interrogation of the
756 interfaces of human tumor and autologous human antitumor immunity in a small animal model.
757 Together, fully activated effector and exhausted-like human $CD8^+$ T cells directly mediate
758 anticancer activity. Our data support clinical exploration of exhausted-like effector $CD8^+$ T cell
759 subsets alongside the recently more favored stem-cell like phenotype for use in adoptive
760 transfer and engineered T cell therapies.
761
762
763
764
765
766
767
768
769
770
771
772
773
774
775
776
777
778
779
780
781

References

1. Simoni Y, Becht E, Fehlings M, Loh CY, Koo SL, Teng KWW, et al. Bystander CD8+ T cells are abundant and phenotypically distinct in human tumour infiltrates. Nature. 2018 May;557(7706):575–9.
2. Scheper W, Kelderman S, Fanchi LF, Linnemann C, Bendle G, de Rooij MAJ, et al. Low and variable tumor reactivity of the intratumoral TCR repertoire in human cancers. Nat Med. 2019 Jan;25(1):89–94.
3. Lan X, Zebley CC, Youngblood B. Cellular and molecular waypoints along the path of T cell exhaustion. Sci Immunol. 2023 Sep;8(87):eadg3868.
4. Lowery FJ, Krishna S, Yossef R, Parikh NB, Chatani PD, Zacharakis N, et al. Molecular signatures of antitumor neoantigen-reactive T cells from metastatic human cancers. Science. 2022 Feb 25;375(6583):877–84.
5. Oliveira G, Wu CJ. Dynamics and specificities of T cells in cancer immunotherapy. Nat Rev Cancer. 2023 May;23(5):295–316.
6. Korman AJ, Garrett-Thomson SC, Lonberg N. The foundations of immune checkpoint blockade and the ipilimumab approval decennial. Nat Rev Drug Discov. 2022 Jul;21(7):509–28.
7. Ribas A, Wolchok JD. Cancer immunotherapy using checkpoint blockade. Science. 2018 Mar 23;359(6382):1350–5.
8. Powles T, Yuen KC, Gillessen S, Kadel EE, Rathkopf D, Matsubara N, et al. Atezolizumab with enzalutamide versus enzalutamide alone in metastatic castration-resistant prostate cancer: a randomized phase 3 trial. Nat Med. 2022 Jan;28(1):144–53.
9. Guan X, Polesso F, Wang C, Sehrawat A, Hawkins RM, Murray SE, et al. Androgen receptor activity in T cells limits checkpoint blockade efficacy. Nature. 2022 Jun;606(7915):791–6.
10. Palmer AC, Izar B, Hwangbo H, Sorger PK. Predictable Clinical Benefits without Evidence of Synergy in Trials of Combination Therapies with Immune-Checkpoint Inhibitors. Clin Cancer Res. 2022 Jan 15;28(2):368–77.
11. Zong W, Rahman T, Zhu L, Zeng X, Zhang Y, Zou J, et al. Transcriptomic congruence analysis for evaluating model organisms. Proc Natl Acad Sci U S A. 2023 Feb 7;120(6):e2202584120.
12. Gilbertson SE, Walter HC, Gardner K, Wren SN, Vahedi G, Weinmann AS. Topologically associating domains are disrupted by evolutionary genome rearrangements forming species-specific enhancer connections in mice and humans. Cell Rep. 2022 May 3;39(5):110769.
13. Medetgul-Ernar K, Davis MM. Standing on the shoulders of mice. Immunity. 2022 Aug 9;55(8):1343–53.
14. Dong MB, Wang G, Chow RD, Ye L, Zhu L, Dai X, et al. Systematic Immunotherapy Target Discovery Using Genome-Scale In Vivo CRISPR Screens in CD8 T Cells. Cell. 2019 Aug 22;178(5):1189-1204.e23.
15. Chen Z, Arai E, Khan O, Zhang Z, Ngiow SF, He Y, et al. In vivo CD8+ T cell CRISPR screening reveals control by Fli1 in infection and cancer. Cell. 2021 Mar 4;184(5):1262-1280.e22.
16. Puig-Saus C, Sennino B, Peng S, Wang CL, Pan Z, Yuen B, et al. Neoantigen-targeted CD8+ T cell responses with PD-1 blockade therapy. Nature. 2023 Mar;615(7953):697–704.
17. De La Rochere P, Guil-Luna S, Decaudin D, Azar G, Sidhu SS, Piaggio E. Humanized Mice for the Study of Immuno-Oncology. Trends Immunol. 2018 Sep;39(9):748–63.
18. Hiwarkar P, Qasim W, Ricciardelli I, Gilmour K, Quezada S, Saudemont A, et al. Cord

blood T cells mediate enhanced antitumor effects compared with adult peripheral blood T cells. Blood. 2015 Dec 24;126(26):2882–91.
19. Chijioke O, Müller A, Feederle R, Barros MHM, Krieg C, Emmel V, et al. Human natural killer cells prevent infectious mononucleosis features by targeting lytic Epstein-Barr virus infection. Cell Rep. 2013 Dec 26;5(6):1489–98.
20. Gros A, Tran E, Parkhurst MR, Ilyas S, Pasetto A, Groh EM, et al. Recognition of human gastrointestinal cancer neoantigens by circulating PD-1+ lymphocytes. J Clin Invest. 2019 Nov 1;129(11):4992–5004.
21. Puccio S, Grillo G, Alvisi G, Scirgolea C, Galletti G, Mazza EMC, et al. CRUSTY: a versatile web platform for the rapid analysis and visualization of high-dimensional flow cytometry data. Nat Commun. 2023 Sep 4;14(1):5102.
22. Chen S, Zhou Y, Chen Y, Gu J. fastp: an ultra-fast all-in-one FASTQ preprocessor. Bioinformatics. 2018 Sep 1;34(17):i884–90.
23. Bray NL, Pimentel H, Melsted P, Pachter L. Near-optimal probabilistic RNA-seq quantification. Nat Biotechnol. 2016 May;34(5):525–7.
24. Love MI, Huber W, Anders S. Moderated estimation of fold change and dispersion for RNA-seq data with DESeq2. Genome Biol. 2014 Dec;15(12):550.
25. Hao Y, Stuart T, Kowalski MH, Choudhary S, Hoffman P, Hartman A, et al. Dictionary learning for integrative, multimodal and scalable single-cell analysis. Nat Biotechnol. 2023 May 25;
26. Dobin A, Davis CA, Schlesinger F, Drenkow J, Zaleski C, Jha S, et al. STAR: ultrafast universal RNA-seq aligner. Bioinformatics. 2013 Jan 1;29(1):15–21.
27. Song L, Cohen D, Ouyang Z, Cao Y, Hu X, Liu XS. TRUST4: immune repertoire reconstruction from bulk and single-cell RNA-seq data. Nat Methods. 2021 Jun;18(6):627–30.
28. Team I. immunarch: an R package for painless bioinformatics analysis of T-cell and B-cell immune repertoires. Zenodo. 2019;10:5281.
29. Baazim H, Antonio-Herrera L, Bergthaler A. The interplay of immunology and cachexia in infection and cancer. Nat Rev Immunol. 2022 May;22(5):309–21.
30. Utzschneider DT, Charmoy M, Chennupati V, Pousse L, Ferreira DP, Calderon-Copete S, et al. T Cell Factor 1-Expressing Memory-like CD8(+) T Cells Sustain the Immune Response to Chronic Viral Infections. Immunity. 2016 Aug 16;45(2):415–27.
31. van der Leun AM, Thommen DS, Schumacher TN. CD8+ T cell states in human cancer: insights from single-cell analysis. Nat Rev Cancer. 2020 Apr;20(4):218–32.
32. Naulaerts S, Datsi A, Borras DM, Antoranz Martinez A, Messiaen J, Vanmeerbeek I, et al. Multiomics and spatial mapping characterizes human CD8+ T cell states in cancer. Sci Transl Med. 2023 Apr 12;15(691):eadd1016.
33. Giles JR, Globig AM, Kaech SM, Wherry EJ. CD8+ T cells in the cancer-immunity cycle. Immunity. 2023 Oct 10;56(10):2231–53.
34. Rahim MK, Okholm TLH, Jones KB, McCarthy EE, Liu CC, Yee JL, et al. Dynamic CD8+ T cell responses to cancer immunotherapy in human regional lymph nodes are disrupted in metastatic lymph nodes. Cell. 2023 Mar;186(6):1127-1143.e18.
35. Prokhnevska N, Cardenas MA, Valanparambil RM, Sobierajska E, Barwick BG, Jansen C, et al. CD8+ T cell activation in cancer comprises an initial activation phase in lymph nodes followed by effector differentiation within the tumor. Immunity. 2023 Jan 10;56(1):107-124.e5.
36. Virassamy B, Caramia F, Savas P, Sant S, Wang J, Christo SN, et al. Intratumoral CD8+ T cells with a tissue-resident memory phenotype mediate local immunity and immune checkpoint responses in breast cancer. Cancer Cell. 2023 Mar;41(3):585-601.e8.
37. Wolfl M, Kuball J, Ho WY, Nguyen H, Manley TJ, Bleakley M, et al. Activation-induced expression of CD137 permits detection, isolation, and expansion of the full repertoire of

CD8+ T cells responding to antigen without requiring knowledge of epitope specificities. Blood. 2007 Jul 1;110(1):201–10.
38. Ye Q, Song DG, Poussin M, Yamamoto T, Best A, Li C, et al. CD137 accurately identifies and enriches for naturally occurring tumor-reactive T cells in tumor. Clin Cancer Res. 2014 Jan 1;20(1):44–55.
39. Parkhurst M, Gros A, Pasetto A, Prickett T, Crystal JS, Robbins P, et al. Isolation of T-Cell Receptors Specifically Reactive with Mutated Tumor-Associated Antigens from Tumor-Infiltrating Lymphocytes Based on CD137 Expression. Clin Cancer Res. 2017 May 15;23(10):2491–505.
40. Gros A, Robbins PF, Yao X, Li YF, Turcotte S, Tran E, et al. PD-1 identifies the patient-specific $CD8^+$ tumor-reactive repertoire infiltrating human tumors. J Clin Invest. 2014 May;124(5):2246–59.
41. Thommen DS, Koelzer VH, Herzig P, Roller A, Trefny M, Dimeloe S, et al. A transcriptionally and functionally distinct PD-1+ CD8+ T cell pool with predictive potential in non-small-cell lung cancer treated with PD-1 blockade. Nat Med. 2018 Jul;24(7):994–1004.
42. Duhen T, Duhen R, Montler R, Moses J, Moudgil T, de Miranda NF, et al. Co-expression of CD39 and CD103 identifies tumor-reactive CD8 T cells in human solid tumors. Nat Commun. 2018 Jul 13;9(1):2724.
43. Yeong J, Suteja L, Simoni Y, Lau KW, Tan AC, Li HH, et al. Intratumoral CD39+CD8+ T Cells Predict Response to Programmed Cell Death Protein-1 or Programmed Death Ligand-1 Blockade in Patients With NSCLC. J Thorac Oncol. 2021 Aug;16(8):1349–58.
44. Lee YJ, Kim JY, Jeon SH, Nam H, Jung JH, Jeon M, et al. CD39+ tissue-resident memory CD8+ T cells with a clonal overlap across compartments mediate antitumor immunity in breast cancer. Sci Immunol. 2022 Aug 26;7(74):eabn8390.
45. Palomero J, Panisello C, Lozano-Rabella M, Tirtakasuma R, Díaz-Gómez J, Grases D, et al. Biomarkers of tumor-reactive CD4+ and CD8+ TILs associate with improved prognosis in endometrial cancer. J Immunother Cancer. 2022 Dec;10(12):e005443.
46. Chow A, Uddin FZ, Liu M, Dobrin A, Nabet BY, Mangarin L, et al. The ectonucleotidase CD39 identifies tumor-reactive CD8+ T cells predictive of immune checkpoint blockade efficacy in human lung cancer. Immunity. 2023 Jan 10;56(1):93-106.e6.
47. Buggert M, Price DA, Mackay LK, Betts MR. Human circulating and tissue-resident memory CD8+ T cells. Nat Immunol. 2023 Jul;24(7):1076–86.
48. Sekine T, Perez-Potti A, Nguyen S, Gorin JB, Wu VH, Gostick E, et al. TOX is expressed by exhausted and polyfunctional human effector memory CD8+ T cells. Sci Immunol. 2020 Jul 3;5(49):eaba7918.
49. Bozorgmehr N, Okoye I, Oyegbami O, Xu L, Fontaine A, Cox-Kennett N, et al. Expanded antigen-experienced CD160+CD8+effector T cells exhibit impaired effector functions in chronic lymphocytic leukemia. J Immunother Cancer. 2021 Apr;9(4):e002189.
50. Okoye I, Xu L, Motamedi M, Parashar P, Walker JW, Elahi S. Galectin-9 expression defines exhausted T cells and impaired cytotoxic NK cells in patients with virus-associated solid tumors. J Immunother Cancer. 2020 Dec;8(2):e001849.
51. Baessler A, Vignali DAA. T Cell Exhaustion. Annu Rev Immunol. 2024 Jan 2;
52. Brenchley JM, Karandikar NJ, Betts MR, Ambrozak DR, Hill BJ, Crotty LE, et al. Expression of CD57 defines replicative senescence and antigen-induced apoptotic death of CD8+ T cells. Blood. 2003 Apr 1;101(7):2711–20.
53. Llaó-Cid L, Roessner PM, Chapaprieta V, Öztürk S, Roider T, Bordas M, et al. EOMES is essential for antitumor activity of CD8+ T cells in chronic lymphocytic leukemia. Leukemia. 2021 Nov;35(11):3152–62.
54. Amaria RN, Postow M, Burton EM, Tetzlaff MT, Ross MI, Torres-Cabala C, et al. Neoadjuvant relatlimab and nivolumab in resectable melanoma. Nature. 2022

Nov;611(7934):155–60.
55. Zhang Y, Chen H, Mo H, Hu X, Gao R, Zhao Y, et al. Single-cell analyses reveal key immune cell subsets associated with response to PD-L1 blockade in triple-negative breast cancer. Cancer Cell. 2021 Dec 13;39(12):1578-1593.e8.
56. Oliveira G, Stromhaug K, Klaeger S, Kula T, Frederick DT, Le PM, et al. Phenotype, specificity and avidity of antitumour CD8+ T cells in melanoma. Nature. 2021 Aug;596(7870):119–25.
57. Guo X, Zhang Y, Zheng L, Zheng C, Song J, Zhang Q, et al. Global characterization of T cells in non-small-cell lung cancer by single-cell sequencing. Nat Med. 2018 Jul;24(7):978–85.
58. Caushi JX, Zhang J, Ji Z, Vaghasia A, Zhang B, Hsiue EHC, et al. Transcriptional programs of neoantigen-specific TIL in anti-PD-1-treated lung cancers. Nature. 2021 Aug;596(7870):126–32.
59. Clarke J, Panwar B, Madrigal A, Singh D, Gujar R, Wood O, et al. Single-cell transcriptomic analysis of tissue-resident memory T cells in human lung cancer. J Exp Med. 2019 Sep 2;216(9):2128–49.
60. Rohaan MW, Borch TH, van den Berg JH, Met Ö, Kessels R, Geukes Foppen MH, et al. Tumor-Infiltrating Lymphocyte Therapy or Ipilimumab in Advanced Melanoma. N Engl J Med. 2022 Dec 8;387(23):2113–25.
61. Mellman I, Chen DS, Powles T, Turley SJ. The cancer-immunity cycle: Indication, genotype, and immunotype. Immunity. 2023 Oct 10;56(10):2188–205.
62. Koppensteiner L, Mathieson L, Pattle S, Dorward DA, O'Connor R, Akram AR. Location of CD39+ T cell subpopulations within tumors predict differential outcomes in non-small cell lung cancer. J Immunother Cancer. 2023 Aug;11(8):e006770.
63. Oliveira G, Egloff AM, Afeyan AB, Wolff JO, Zeng Z, Chernock RD, et al. Preexisting tumor-resident T cells with cytotoxic potential associate with response to neoadjuvant anti-PD-1 in head and neck cancer. Sci Immunol. 2023 Sep 8;8(87):eadf4968.
64. Krishna S, Lowery FJ, Copeland AR, Bahadiroglu E, Mukherjee R, Jia L, et al. Stem-like CD8 T cells mediate response of adoptive cell immunotherapy against human cancer. Science. 2020 Dec 11;370(6522):1328–34.
65. Hanada KI, Zhao C, Gil-Hoyos R, Gartner JJ, Chow-Parmer C, Lowery FJ, et al. A phenotypic signature that identifies neoantigen-reactive T cells in fresh human lung cancers. Cancer Cell. 2022 May 9;40(5):479-493.e6.
66. Mestas J, Hughes CCW. Of mice and not men: differences between mouse and human immunology. J Immunol. 2004 Mar 1;172(5):2731–8.

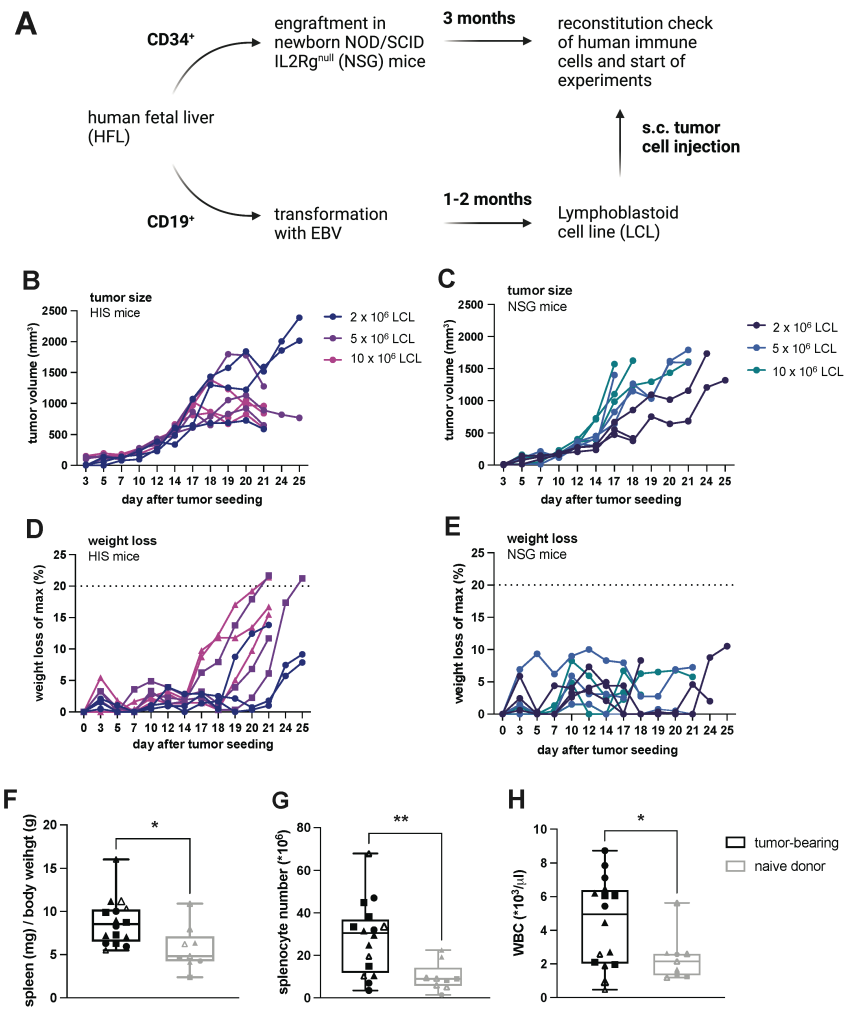

Figure 1: LCL tumor growth kinetics and weight loss in autologous HIS mice and NSG mice. LCL tumors were injected subcutaneously into the flank of mice and tumor size was assessed by calipering. **A**, schematic of generation of HIS mice and autologous tumor cells and subsequent injection in HIS mice. **B**, tumor volume in HIS mice after implantation of the indicated number of LCLs. **C,** Tumor volume in NSG mice after implantation of the indicated number of LCLs. (D, E) Relative weight loss calculated based on the maximum weight during the experiment after tumor cell implantation of the indicated number of LCLs in HIS (**D**) or NSG (**E**) mice. **F**, ratio of spleen weight (mg) to body weight (g), **G**, total splenocyte number and **H**, white blood cell count in HIS mice injected with 5 x 10^6 autologous LCL tumor cells or non-tumor bearing HIS mice (naïve) sacrificed 15-20 days after tumor implantation. B-E, n=3 per tumor cell number, F-H, n(tumor-bearing)=16, n(naïve)=9 from 4 individual experiments,

marked by individual symbols. Unpaired t-test, data shown as box and whiskers with the box from the 25-75 percentile and the median is shown as a line within the box; whiskers are shown from minimum to maximum data point.

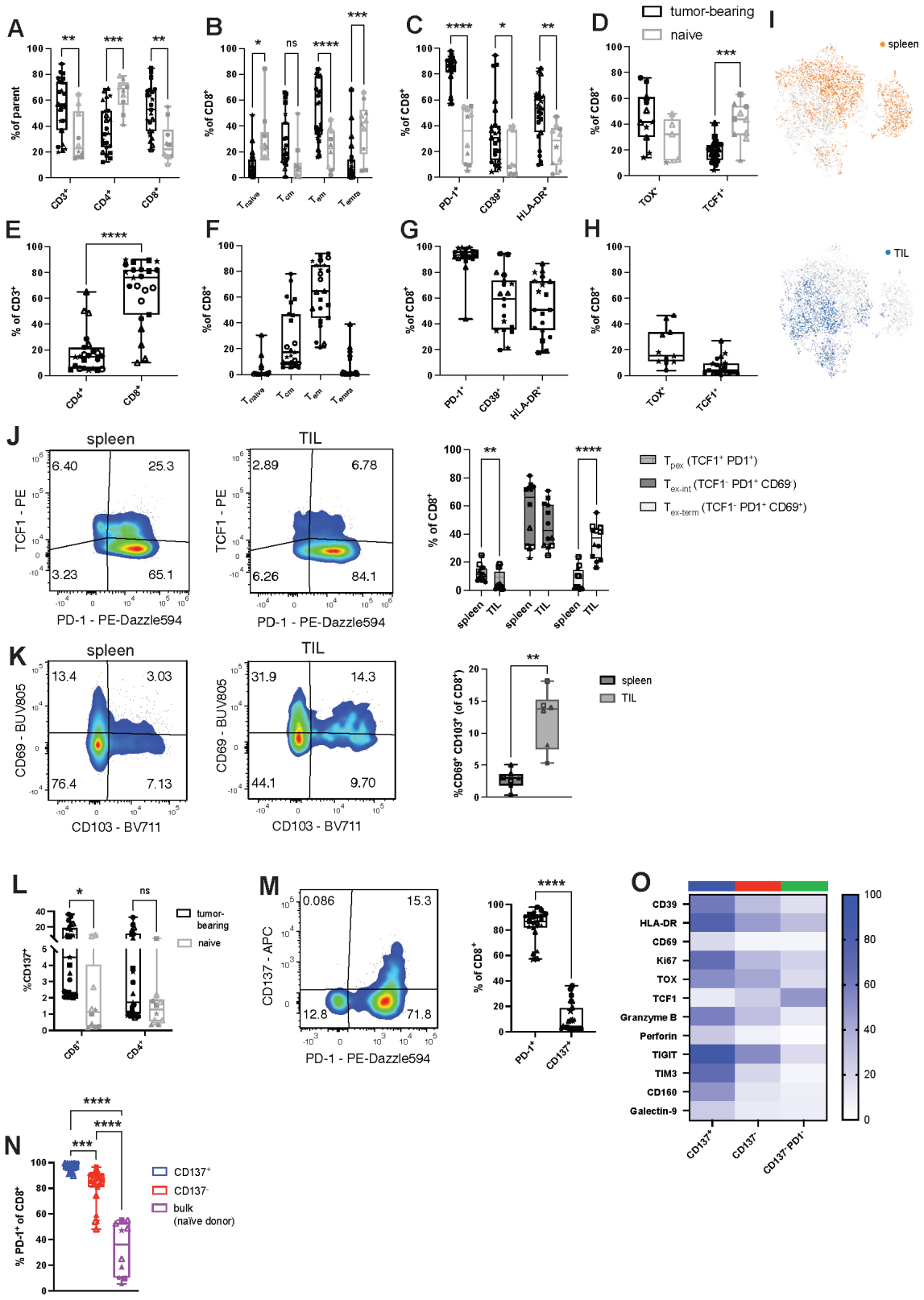

Figure 2: T cell response in tumor-bearing HIS mice. Splenocytes (A-D) and tumor-infiltrating lymphocytes (TIL) (E-H) were isolated from HIS mice 16-18 days after tumor implantation and analyzed by flow cytometry. **A,** frequency of splenic T cells in tumor-bearing

or naïve HIS mice; parent population refers to frequency (%) of $CD3^+$ T cells within human $CD45^+$ cells and $CD4^+$ and $CD8^+$ T cells within $CD3^+$ T cells. **B**, $CD8^+$ T cell differentiation defined as $T_{naïve}$ ($CD45RA^+CD62L^+$), T_{CM} ($CD45RA^-CD62L^+$), T_{EM} ($CD45RA^-CD62L^-$), T_{EMRA} ($CD45RA^+CD62L^-$) in tumor-bearing or naïve HIS mice. **C-D**, expression of indicated markers on $CD8^+$ T cells from spleen of tumor-bearing or naïve HIS mice. **E,** frequency of $CD4^+$ and $CD8^+$ T cells within TILs, gated on total $CD3^+$ T cells. **F,** $CD8^+$ T cell differentiation within TILs. **G-H,** expression of indicated markers on $CD8^+$ T cells within TILs. **I**, UMAP of $CD8^+$ T cells from spleen and TIL of tumor-bearing HIS mice, colored for tissue of origin. **J**, expression of PD-1 and TCF1 in spleen and TIL of tumor-bearing HIS mice and quantification of $CD8^+$ T_{pex} ($TCF1^+PD1^+$), $T_{ex\text{-}int}$ ($TCF1^-PD1^+CD69^-$), $T_{ex\text{-}term}$ ($TCF1^-PD1^+CD69^+$) in both tissues. **K**, expression of CD69 and CD103 in spleen and tumor of tumor-bearing HIS mice and quantification of T_{RM}-like ($CD69^+CD103^+$) $CD8^+$ T cells in both tissues. **L,** expression of CD137 on splenic $CD8^+$ and $CD4^+$ T cells of tumor-bearing or naïve HIS mice. **M,** expression and quantification of PD-1 and CD137 on splenic $CD8^+$ T cells of tumor-bearing HIS mice. **N**, expression of PD-1 on splenic $CD137^+$ or $CD137^-$ $CD8^+$ T cells in tumor-bearing HIS mice or bulk $CD8^+$ T cells from naïve HIS mice. **O**, expression of individual markers on splenic $CD8^+$ T cell populations from tumor-bearing HIS mice based on expression of CD137 and PD-1. Data are pooled from at least 3 independent experiments, n=10-23 mice per group. For each experiment, a different HPC donor was used for HIS mouse reconstitution and generation of autologous tumor. Significance by paired t-test, one-way ANOVA or 2way ANOVA, as appropriate. Data from individual experiments are indicated by different symbols, with individual mice from the same experiment indicated by the same symbol.

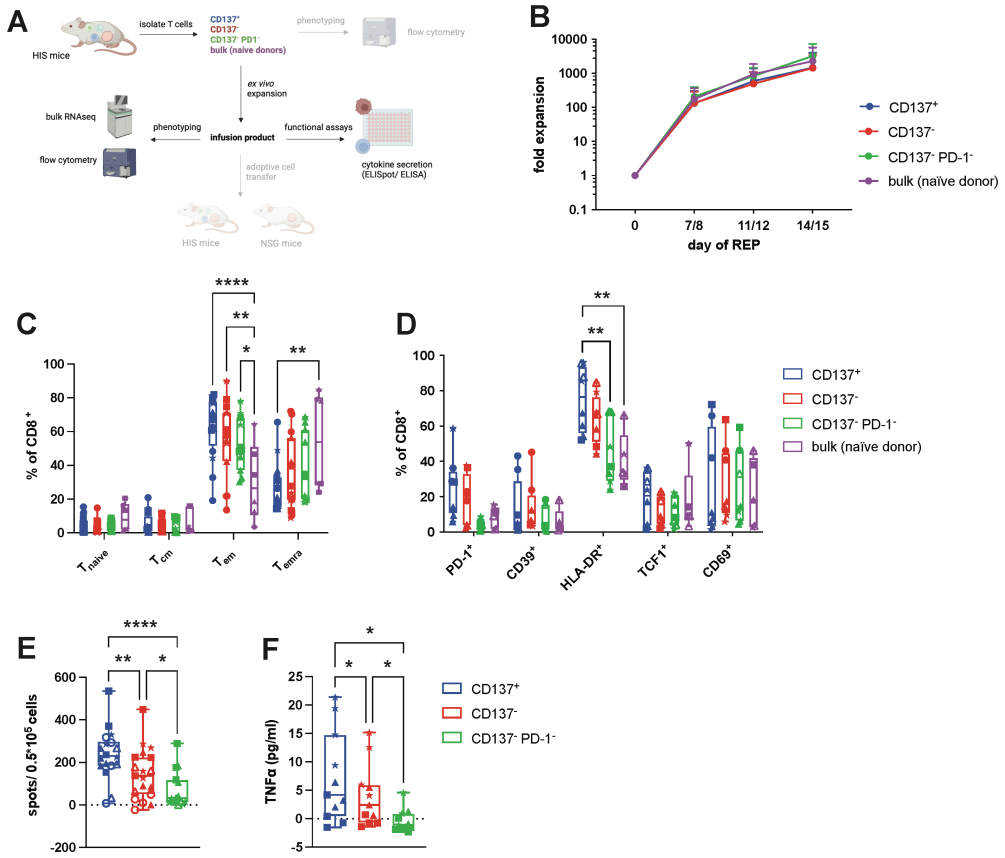

Figure 3: Exhausted-like human CD8$^+$ T cells derived from tumor-bearing HIS mice can be expanded *ex vivo* and exhibit superior tumor-specific cytokine production. A, schematic of generation, expansion and characterization of T cells from HIS mice bearing autologous LCL tumors. **B**, fold expansion of FACS sorted splenic CD8$^+$ T cells from tumor-bearing HIS mice (CD137$^+$, CD137$^-$ and CD137$^-$PD1$^-$) or naïve HIS mice (bulk). **C**, CD8$^+$ T cell differentiation after *ex vivo* expansion defined as $T_{naïve}$ (CD45RA$^+$CD62L$^+$), T_{CM} (CD45RA$^-$CD62L$^+$), T_{EM} (CD45RA$^-$CD62L$^-$), T_{EMRA} (CD45RA$^+$CD62L$^-$). **D**, expression of indicated markers after *ex vivo* expansion. **E**, IFN-γ ELISpot of expanded T cells in 5:1 (E:T) co-culture with autologous LCL tumor cells for 24 hours. Spot count is normalized to the spots produced by expanded CD8$^+$ bulk T cells from naïve HIS mice. **F**, TNFα ELISA of supernatant of expanded T cells in co-culture (5:1, E:T) with autologous LCL tumor cells for 24 hours. TNFα concentration is normalized to the TNFα secretion from expanded CD8$^+$ bulk T cells derived from naïve mice. Data are pooled from at least 3 independent experiments, n=6-19 mice per

group. For each experiment, a different HPC donor was used for HIS mouse reconstitution and generation of autologous tumor. Significance by mixed-effects analysis (paired), RM one-way ANOVA or 2way ANOVA, as appropriate. Data from individual experiments are indicated by different symbols, with individual mice from the same experiment indicated by the same symbol.

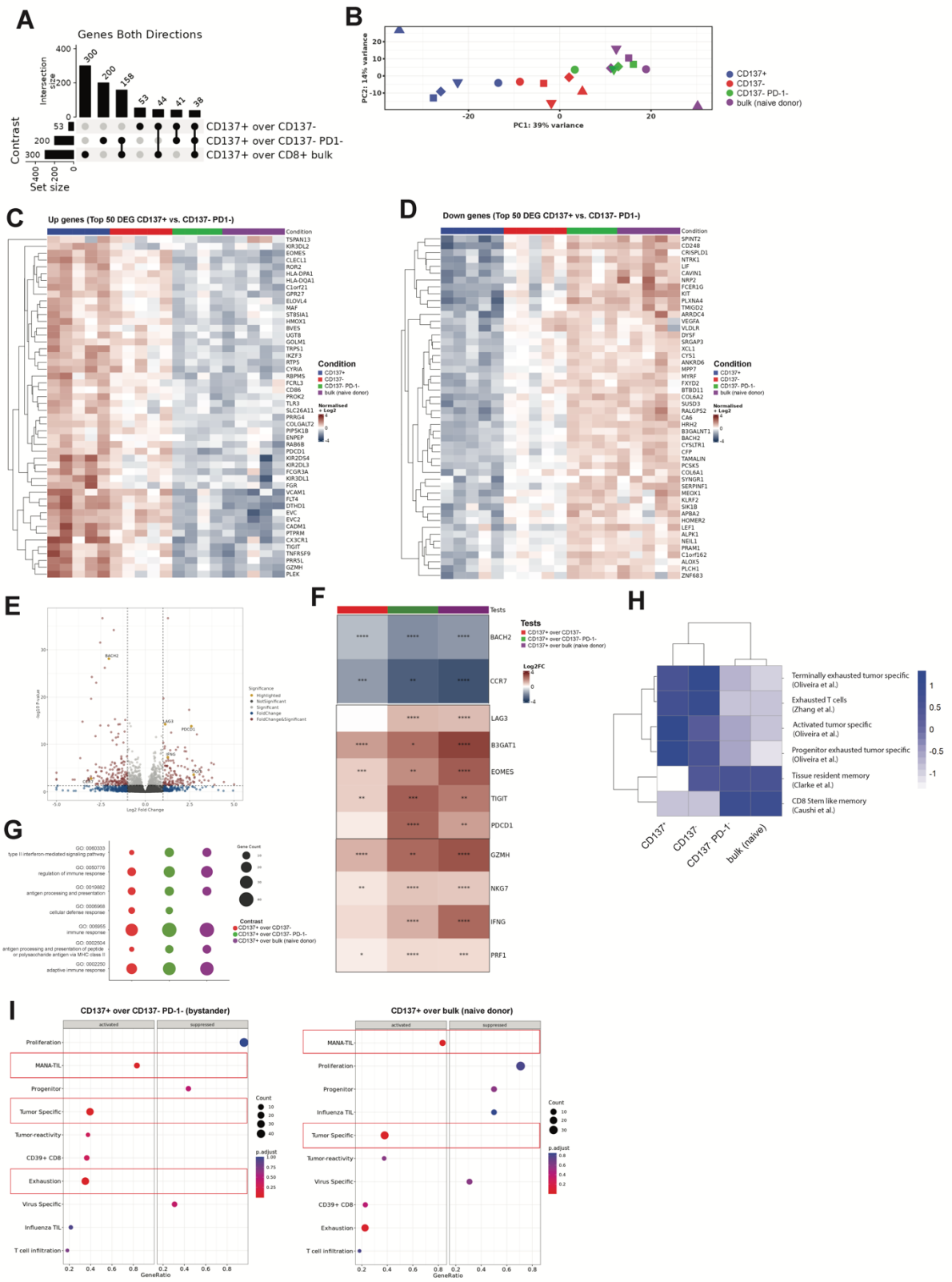

Figure 4: Transcriptomic profiling of tumor-reactive CD137^{+} CD8^{+} T cells

Transcriptome analysis and pathway analysis of expanded CD8^{+} T cells from tumor-bearing HIS mice (CD137^{+}, CD137^{-} and CD137^{-}PD1^{-}) or naïve HIS mice (bulk). **A,** Upset plot

(intersect) showing **number** of differentially expressed genes between groups in bulk RNAseq. p(FDR) < 0.05, log2 FC > 1.5. **B**, PCA plot of RNAseq showing PC1 and PC2. **C,** Top 50 upregulated and **D,** downregulated genes of T cell subsets based on the DEG between $CD137^+$ vs. $CD137^-PD1^-$ $CD8^+$ T cells. p(FDR) < 0.05, log2 FC > 1.5. **E,** Volcano plot showing DEG between $CD137^+$ and $CD137^-PD1^-$ $CD8^+$ T cells with genes of interest highlighted in yellow. **F**, differential expression of genes of interest between groups. **G**, Overrepresentation analysis (ORA) of upregulated pathways in $CD137^+$ $CD8^+$ T cells. **H**, Gene module score analysis of published signatures described on the right. **I**, Gene set enrichment analysis (GSEA) of signatures described on the y-axis. Gene ratio (# genes related to GO term / total number of sig genes) is displayed on the x-axis. Signatures with an adjusted p-value <0.05 are highlighted with a red box. Shown are data from 4-5 individual experiments, each experiment with different human HPC donor for reconstitution of HIS mice and autologous tumor.

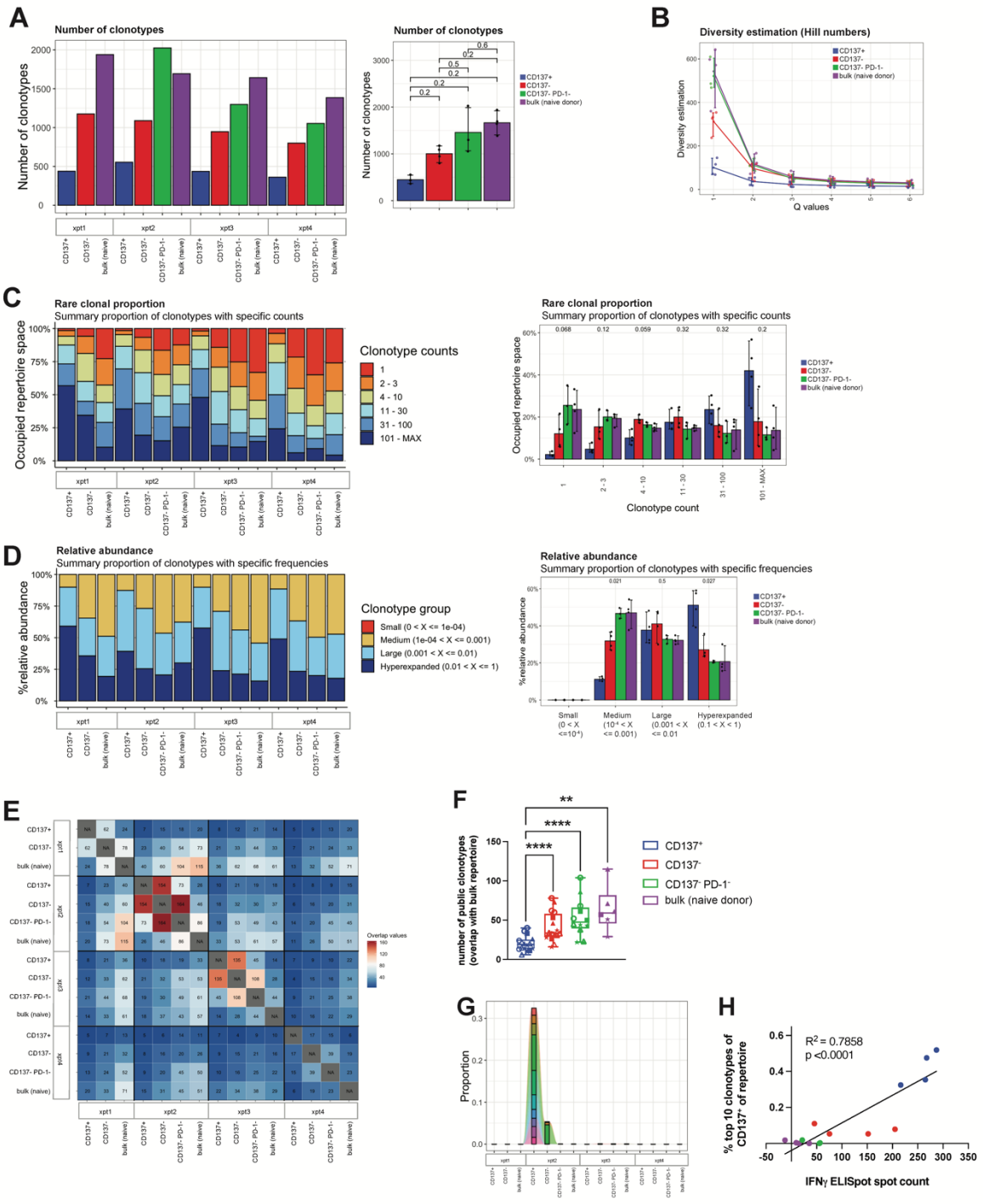

Figure 5: TCR profiling of tumor-reactive CD137$^+$ CD8$^+$ T cells. A, total number of individual clonotypes found per population. Left: data from individual experiments, right: pooled data for group analysis. Wilcoxon test. **B,** TCR (CDR3 of *TRA*, *TRB*, *TRG* and *TRD*) sequence sample diversity estimation using Hill numbers method, with Q=1 describing the Shannon diversity. **C,** rare clonal proportion showing the occupied repertoire space by clonotypes with defined counts (1, 2-3, 4-10, etc.). Left: data from individual experiments, right: pooled data for group

analysis. Wilcoxon test. **D,** relative abundance of clonotypes with defined frequencies (size). Left: data from individual experiments, right: pooled data for group analysis. Wilcoxon test. **E,** repertoire overlap analysis cross-comparing every population from every experiment (each with different donor). **F**, repertoire overlap comparing the repertoire of bulk $CD8^+$ T cells from naïve HIS mice to the populations from tumor-bearing HIS mice from individual experiments (each with different donor; data from individual experiments are indicated by different symbols). Mixed effects analysis with Tukey's multiple comparisons test. **G**, tracking of clonotypes over populations. The top 10 most abundant clonotypes of the TCR repertoire of $CD137^+$ $CD8^+$ T cells from one representative experiment are shown. **H**, proportion of the top 10 most abundant clonotypes (from repertoires of $CD137^+$ $CD8^+$ T cells) in the repertoire of all populations, correlated with the spot count of IFN-γ ELISpot. Shown are data from 4 individual experiments, each experiment with different human HPC donor for reconstitution of HIS mice and autologous tumor.

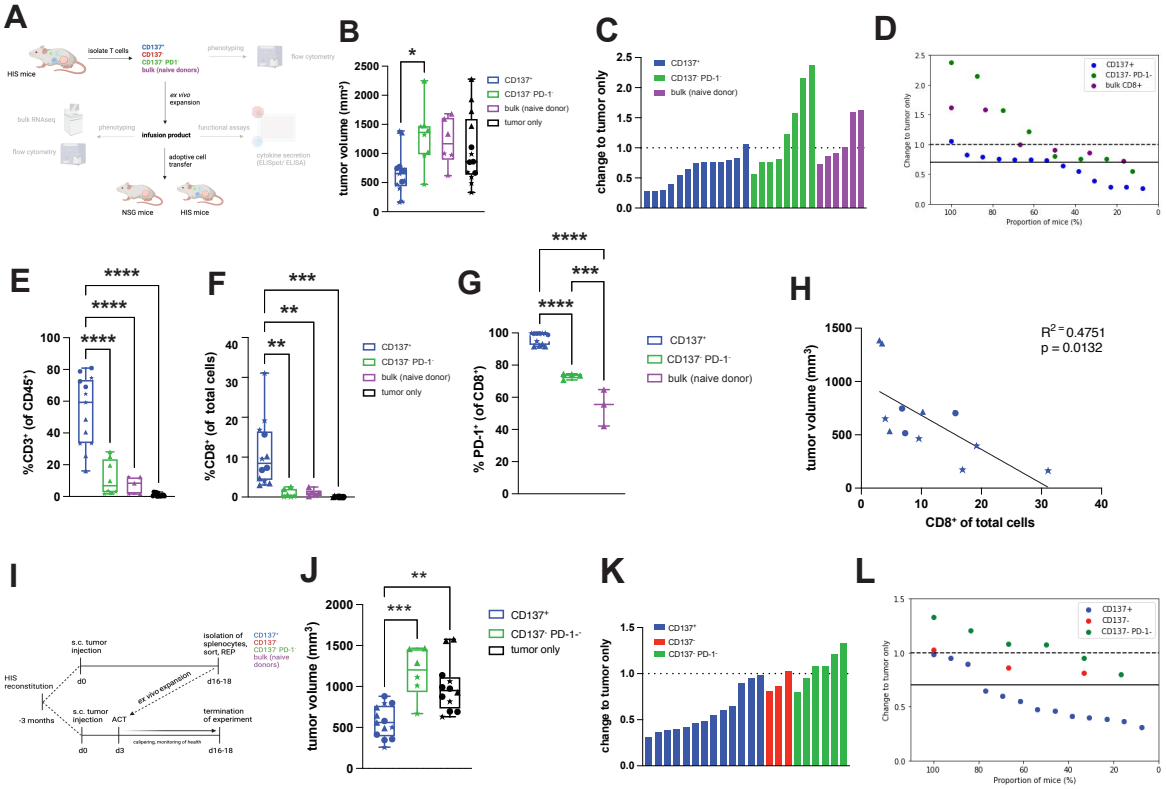

Figure 6: CD137⁺ CD8⁺ T cells from tumor-bearing HIS mice show superior anticancer activity in NSG and HIS recipients bearing autologous tumors. A, schematic of generation of tumor-reactive T cells and subsequent ACT. NSG mice were injected with 2 x 10^6 LCL s.c. in the flank and after three days, 10 x 10^6 *ex vivo* expanded T cells were adoptively transferred intravenously. Transferred T cells and LCL tumors were autologous to each other. **B**, tumor volume on the day of sacrifice in NSG recipient mice after ACT of the indicated cell populations. **C,** waterfall plot of tumor size in NSG recipient mice of ACT on the day of sacrifice relative to the tumor volume of control mice (no ACT). Bars depict individual mice. **D**, proportion of NSG recipient mice showing partial response (≥ 30% tumor reduction compared to control NSG mice) after ACT of the indicated cell population. **E**, frequency of $CD3^+$ T cells (% of human $CD45^+$ cells) in TIL of NSG mice after ACT of the indicated cell populations, measured by flow cytometry. **F**, frequency of $CD8^+$ T cells (% of total cells) in tumors of NSG mice after ACT of the indicated cell populations, measured by immunohistochemistry. **G**, frequency of PD-1 expression on $CD8^+$ T cells in TIL of NSG mice after ACT of the indicated cell populations. **H,** correlation between tumor volume and infiltration of $CD8^+$ T cells

(measured by IHC) in tumors of NSG mice after adoptive transfer of $CD137^+$ $CD8^+$ T cells. **I**, schematic of ACT. $CD137^+$ $CD8^+$ T cells, $CD137^-$ $CD8^+$ T cells and $CD137^-$ $PD\text{-}1^-$ $CD8^+$ T cells were isolated from spleen of tumor-bearing HIS mice or bulk $CD8^+$ T cells from spleen of naïve HIS mice and expanded *ex vivo*. Recipient HIS mice were injected with 2×10^6 LCL s.c. in the flank and after three days, *ex vivo* expanded T cells were adoptively transferred intravenously. Tumor-bearing HIS recipient mice received 2×10^6 T cells without prior conditioning/lymphodepletion. Donor and recipient HIS mice as well as LCL were autologous to each other. **J,** tumor volume on the day of sacrifice in HIS recipient mice after ACT of the indicated cell populations. **K,** waterfall plot of tumor size on the day of sacrifice of HIS mice receiving ACT relative to the tumor volume of control HIS mice (no ACT). Bars depict individual mice. **L**, proportion of HIS recipient mice showing partial response (≥ 30% tumor reduction compared to control HIS mice) after ACT of the indicated cell population. Data are pooled from 1-3 independent experiments, n=3-13 per group. For each experiment, a different HPC donor was used for HIS mouse reconstitution and generation of autologous tumor. Significance by one-way ANOVA. Data from individual experiments are indicated by different symbols, with individual mice from the same experiment indicated by the same symbol.